5641

Studies on the

Assembly, Growth and Related Aspects of

Nanostructures by Isothermal Titration Calorimetry,

Small Angle X-Ray Scattering and Other Techniques

A Thesis

submitted in partial fulfillment of the

requirements of the degree of

Master of Science

as a part of the Integrated Ph.D programme

by

Neenu Varghese

Chemistry and Physics of Materials Unit
Jawaharlal Nehru Centre for Advanced Scientific
Research
(A Deemed University)
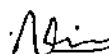Bangalore – 560 064
June 2008

Dedicated To My Parents

DECLARATION

I hereby declare that the matter embodied in this thesis entitled **"Studies on the Assembly, Growth and Related Aspects of Nanostructures by Isothermal Titration Calorimetry, Small Angle X-Ray Scattering and Other Techniques"** is the result of investigations carried out by me under the supervision of Prof. C. N. R. Rao, FRS at the Chemistry and Physics of Materials Unit, Jawaharlal Nehru Centre for Advanced Scientific Research, Bangalore, India and that it has not been submitted elsewhere for the award of any degree or diploma.

In keeping with the general practice in reporting scientific observations, due acknowledgement has been made whenever the work described is based on the findings of other investigators.

Neenu Varghese

CERTIFICATE

I hereby certify that the matter embodied in this thesis entitled " **Studies on the Assembly, Growth and Related Aspects of Nanostructures by Isothermal Titration Calorimetry, Small Angle X-Ray Scattering and Other Techniques**" has been carried out by Ms. Neenu Varghese, at the Chemistry and Physics of Materials Unit, Jawaharlal Nehru Centre for Advanced Scientific Research, Bangalore, India under my supervision and that it has not been submitted elsewhere for the award of any degree or diploma.

Prof. C. N. R. Rao, FRS

(Research Supervisor)

Acknowledgements

Preface

The thesis is divided into four chapters. Chapter 1 gives a brief overview of nanomaterials.

The use of isothermal titration calorimetric (ITC) to study the growth and interactions with ligand molecules of nanomaterials is presented in Chapter 2. The self-assembly of gold nanorods to form chains with two different linkers have been studied using ITC along with UV-visible spectroscopy and transmission electron microscopy. The growth of gold nanocrystals has been investigated with ITC and the heat change associated with the growth was determined. The disintegration gold nanofilm formed at the liquid-liquid interface by various alkanethiols of different chain length have been monitored calorimetry which gave an understanding of dependence of the alkane chain length in disintegrating the film.

In chapter 3, the study of growth kinetics of CdSe and CdS nanocrystals using a variety of techniques such as small angle X-ray scattering (SAXS), transmission electron microscopy, and UV-visible and photoluminescence spectroscopy is described. The growth of the nanocrystals is found to be controlled by a combination of diffusion and reaction at the surface

Chapter 4 deals with the preliminary study of the binding of nucleobases and nucleosides with graphene by isothermal titration calorimetry.

Contents

Chapter 1

Nanomaterials: A brief overview

Introduction

Nanoscience involves the study of properties and phenomena on the scale of 1-100 nm (1 nm = 10^{-9} m). Nanotechnology involves the design, fabrication and application of nanomaterials, and the fundamental understanding of the relationships between physical properties or phenomena and materials dimensions. On nanometer scale, materials or structures may possess new physical properties or exhibit new physical phenomena which vary with change in their size and shape. Nanoscale materials often exhibit behavior that is intermediate between that of a macroscopic solid and an atomic or molecular species. This is partly due to the high surface to volume ratio of these materials and partly due to the size induced quantum confinement of the electrons. Due to these special properties the research on this area is evolving and expanding very rapidly.

The study on nanomaterials is a new subject although they were used from ancient times. Chinese are known to use Au nanoparticles as an inorganic dye to introduce red color into their ceramic porcelains more than thousand years ago [1]. Colloidal gold was used for treatment of arthritis. The secret behind the color of the Lycurgus cup, a roman glass artifact dated to 4 AD, that appears red in transmitted light and green in reflected light was found to be due to Au and Ag nanocrystals impregnated

in glass. Use of colloidal gold has a long history, though a comprehensive study on the preparation and properties of colloidal gold was done in the middle of the 19th century by

Figure 1.1 gold colloids prepared by Michael Faraday

Michael Faraday [2]. He established that several dyes were indeed made of metal particles. After a thorough study of gold sols, Faraday concluded *". . . the gold is reduced in exceedingly fine particles which becoming diffuse, produce a beautiful fluid. . . the various preparations of gold, whether ruby, green, violet or blue. . . consist of that substance in a metallic divided state"*. Thus, colloidal metal particles in sols came to be known as divided metals. Figure 1.1 shows gold colloids prepared by Faraday. Now nanometer scale structures represent a rapidly expanding and challenging area of research that crosses the borders between many areas of physical sciences and engineering due to the ability to see and manipulate matter on the nanoscale and understanding of atomic scale interactions.

1.1 Properties of nanomaterials

In a metal, electrons are highly delocalized over large space (i.e., least confined). This is a result of the fact that the separation between the valence and conduction bands vanishes, giving the metal its conducting properties. As we decrease the size of the metal and confine its electronic motion, the separation between the valence and the conduction bands becomes comparable to or larger than kT, and the metal

becomes a semiconductor. More confinement increases the energy separation further, and the material becomes an insulator. In the size domain at which the metal-to-insulator transition occurs, new properties are expected to be observed which are possessed neither by the metal nor by the molecules or atoms forming the metal [3].

Optical properties

In noble metals, the decrease in size below the electron mean free path (the distance the electron travels between scattering collisions with the lattice centers) gives rise to intense absorption in the visible-near UV [4-7]. This results from the coherent oscillation of the free electrons from one surface of the particle to the other and is called the surface plasmon absorption. A schematic illustration of the electric field component of an incoming light wave inducing a polarization of the free or itinerant electrons with respect to the heavier core is shown in Figure 1.2 [6]. This gives these metallic nanoparticles brilliant color in colloidal solution that intrigued scientists in the 17th century. It was Faraday who showed that the intense color is due to metallic gold in colloidal form [2]. In 1908 Mie explained the phenomena by solving Maxwell's equations for the absorption and scattering of electromagnetic radiation by spherical metallic particles [8]. This theory has been used to calculate the spectra of particles smaller than the wavelength of light for nanoparticles whose metallic dielectric function is known and which are embedded in an environment of known dielectric constant [5, 9, 10]. Colloidal metallic nanoparticles are of interest because of their use as catalysts, photocatalysts, sensors, ferrofluids, and because of their applications in optoelectronics, electronic and magnetic devices [11-14].
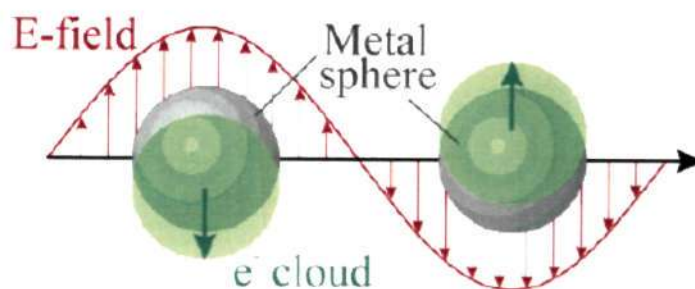
Figure 1.2 Schematic of plasmon oscillation for a sphere, showing the displacement of the conduction electron charge cloud relative to the nuclei [Ref. 6]

The shape dependence of the surface plasmon absorption was studied by Gans [14]. For nanorods two absorption bands are seen: one is due to the coherent electronic oscillation along the short axis (the transverse absorption band), and the other (the longitudinal band) is at a longer wavelength, which is more intense and results from the coherent electronic oscillation along the long axis. UV-visible spectrum of the gold nanorods of aspect ratio 4.1 is shown in Figure 1.3 [15]. The absorption maximum of the latter band is sensitive to the rod length. Transverse band appear at a lower wavelength ($\sim$ 520nm) and longitudinal shifts to longer wavelengths as increase in length of the nanorods.
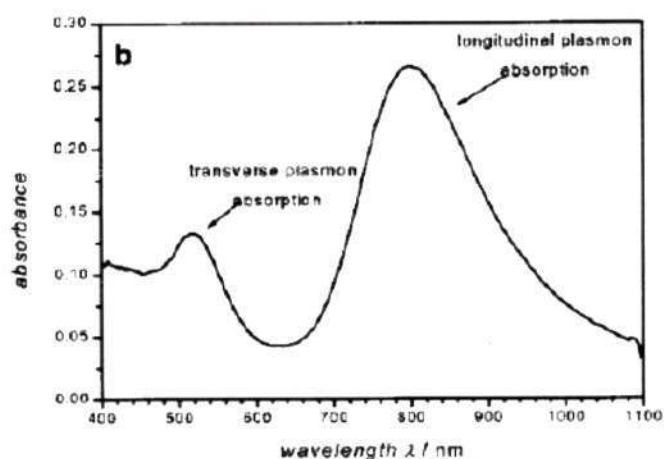
Figure 1.3 UV-vis spectrum of gold nanorods of aspect ratio 4.1

Figure 1.4 shows colors gold nanorods of different aspect ratios and the corresponding optical spectra [16]. This absorption is over 1000 times stronger than the strongest absorption of molecular dyes and is responsible for enhancing other linear and nonlinear processes involving the interaction of these nanoparticles with electromagnetic radiation [17], e.g., fluorescence, surface-enhanced Raman scattering, and second harmonic generation. Furthermore, the fact that the absorption intensity and wavelength maximum of these nanocrystals are sensitive to the dielectric constant of the environment makes them potentially useful as sensors.
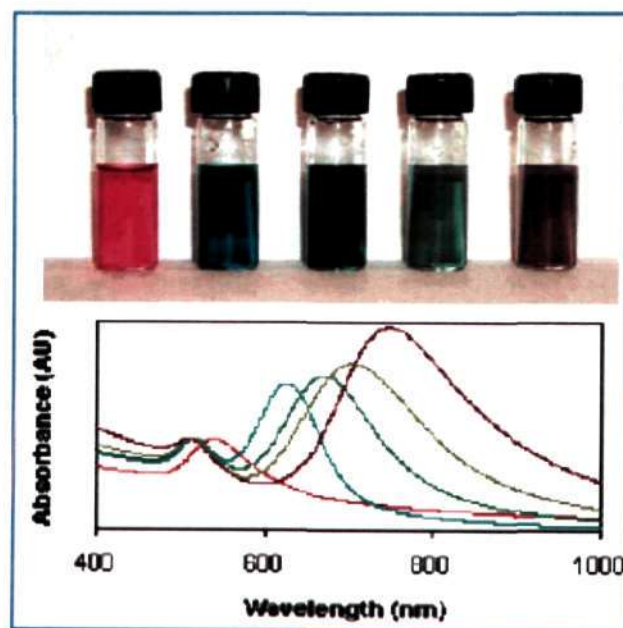
Figure 1.4 Image of photochemically prepared gold nanorods solution, and corresponding UV-vis spectrum [Ref.16].

In semiconductor nanocrystals, changes in optical properties result from the further confinement of the electronic motion to a length scale that is comparable to the mean free path of the electrons in the bulk material. Reduction in nanocrystal-size beyond

the bulk excitonic Bohr radius induces a larger band gap that causes blue-shifts in the
absorption wavelength [18]. The absorption band can be systematically varied across
ranges of a few 100 nm by changing the size of the semiconductor nanocrystal. As an
example, the absorption spectra of CdSe nanocrystals of various sizes are shown in
Figure 1.5 [19]. The excitonic nature of the absorption band permits direct correlation of
the band gap of the semiconductor nanocrystal with the absorption edge.
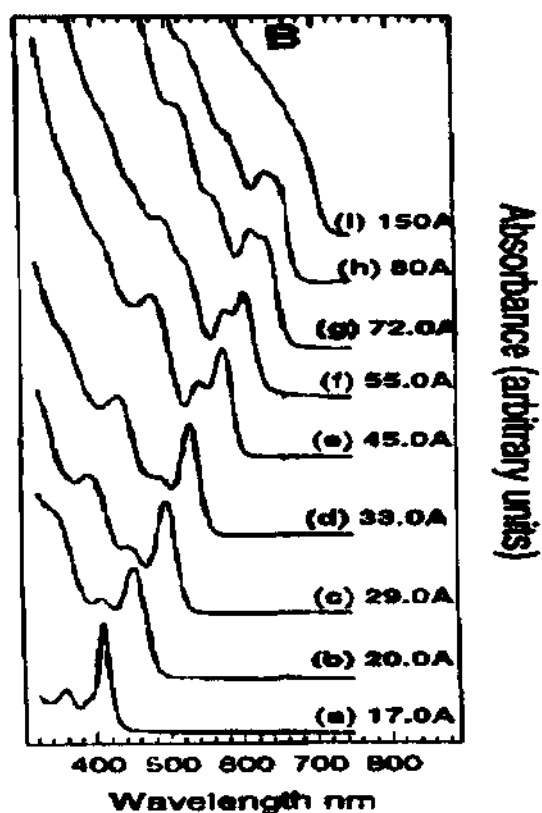
Figure 1.5 Optical absorption spectra of
CdSe nanocrystals with varying diameters
[Ref.19].

In addition to the interesting absorption properties, the semiconductor
nanocrystals also exhibit strong photoluminescence (PL) properties due to the non-
radiative recombination of the electron-hole pairs. The emission from monodisperse

semiconductor nanocrystals such as CdSe is intense, narrow and can be brought about by excitation in a broad range of wavelengths [20]. The emission can be tuned by altering the diameter of the nanocrystal. These properties have led to the exploration of a wide range of applications for luminescent semiconductor nanocrystals [21].

1.2 Self assembly of nanomaterials

The development of rational approaches for multidimensional interconnection of nanoscale building blocks into desired nanostructures is a significant challenge in the realization of advanced nanodevices [22, 23]. Self assembly driven by various interactions is an effective strategy for forming versatile soft nanocrystal assembly motifs [24-28]. Understanding factors governing the creation of nanocrystal assemblies would allow the design of desired nanostructures for optical, microelectronic, chemical and biological applications [29].

Monofunctionalized nanoparticles can be used as molecular building blocks to react with other chemicals such as polymers, to give rise to nanomaterials linked with covalent bonds [30]. Nanoparticles encapsulated within cross-linked polymers undergo a sphere to chain transition induced by the micelle transition [31]. Ordered self-assembly of Au nanocrystals and Fe_2MnO_4 nanocubes into two- and three-dimensional (3-D) arrays from water soluble nanocrystal micelles have been observed [32]. The method involves drying water soluble Au nanocrystal micelles synthesized by a surfactant encapsulation technique. A spontaneous formation of nanoparticle strip patterns have been observed on dewetting a dilute film of polymer coated nanoparticles floating on a water surface [33]. Au nanoparticle monolayers and multilayers have been constructed on a gold surface

using coordination chemistry of metal ions [34]. Au nanoparticle networks can be prepared by functionalizing them with azobenzene derivatives [35]. Gold nanocrystals produced electrochemically in the presence of PVP spontaneously order into 1D or 2D arrays [36]. Hybridization of branched DNA trimers and Au nanoparticle DNA conjugates has been employed to produce discrete self-assembled nanoparticle dendrimers [37]. *The effect of disorder on the phase behavior of DNA-linked gold nanoparticle assemblies has been studied* [38]. Variation in the length of the DNA linker results in different melting temperatures of the DNA-linked nanoparticle assemblies.

By controlling the size distribution of magnetic Co nanocrystals, mesoscopic patterns with columnar and labyrinth structures are achieved [39]. Self-assembly of triangular and hexagonal CdS nanocrystals into complex structures such as rods and arrows has been observed [40]. Ring-like structures of semiconductors are found to occur by the self-assembly of nanocrystals in aqueous media [41, 42]. Self-assembly of NRs is also controllable via careful control over experimental conditions such as the concentration, pH, ion strength and size distribution of NRs as well as the parameters affecting water evaporation [43–47] or by virtue of Langmuir–Blodgett [LB] techniques [48]. Self-assembly of Au nanorods driven by surfactants [49] and DNA molecules [50] have been demonstrated. Figure 1.6 shows self assembled gold nanorods by DNA hybridization [50].

Figure 1.6 Transmission electron micrographs of bundles of DNA-linked gold nanorods. [Ref. 50]

End to end assembly of gold nanorods

The assembly of nanomaterial across extended length scales is a key challenge to the integration of functional nanodevices and nanomaterials. The real value of nanotechnology is to develop advanced nanodevices of superior function and properties. While most of the ordered structures published recently are based on colloidal particles [51–56], nanorods with anisotropic properties and longitudinal mode on optical excitations have also attracted great attention. The assembly of gold nanorods (GNRs) is attractive for several important applications, including surface-enhanced Raman scattering (SERS) and fluorescence sensing [57-59]. El-Sayed *et al* have organized GNRs into one-, two- and three-dimensional structures by controlling the evaporation of solvent [60]. Murphy *et al* have demonstrated that electrostatic interactions lead to the organization of GNRs into self-assembled monolayers [61, 62].

The structure of the gold nanorods plays an important role in their end to end self assembly. Figure 1.7 shows a high-resolution TEM image of an Au nanorod oriented along [110].
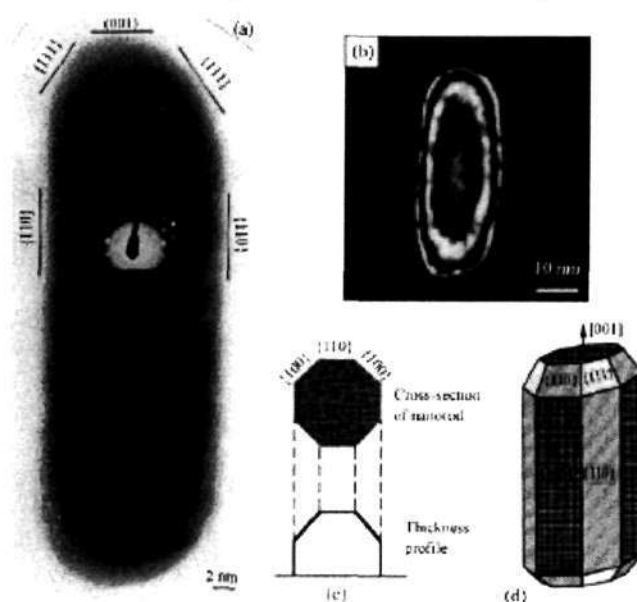
Figure 1.7 (a) High-resolution TEM image of a gold nanorod showing the facetted crystal structure of the rod. (b) Dark-field TEM image of a gold nanorod. (c) Cross-section and the corresponding profile of crystal thickness and (d) structural model [Ref. 63].

The facets enclosing the nanorods are identified from the electron diffraction pattern, and the side facets are {110} and {100} with approximately equivalent surface area and the growth direction is [001]. The ends of the nanorods are terminated by the (001) and {111} facets of small areas [63]. The surfactant cetyl trimethylammonium bromide (CTAB) preferentially binds to the {100} faces, along the length of the rods, compared to the end {111} Au faces, due to the size of the CTAB head group [64, 65]. The binding of the large $[NMe3]^+$ headgroup of CTAB and associated long alkyl chain can be more readily accommodated at the {100} side edges than within the plane of individual close-packed {111} faces, where the Au-Au spacings are too small to facilitate epitaxy. As the nanorods grow in length, the area of the side faces increases, and this facilitate the assembly of a bilayer of CTAB molecules as shown in Figure 1.8 at the crystal surface [66]. This makes the binder molecule unsuccessful at displacing the CTAB bound to the length of the gold nanorods, and thus it preferentially bound to the {111} ends of the rods, resulting in preferential end-to-end linkages [64, 66].
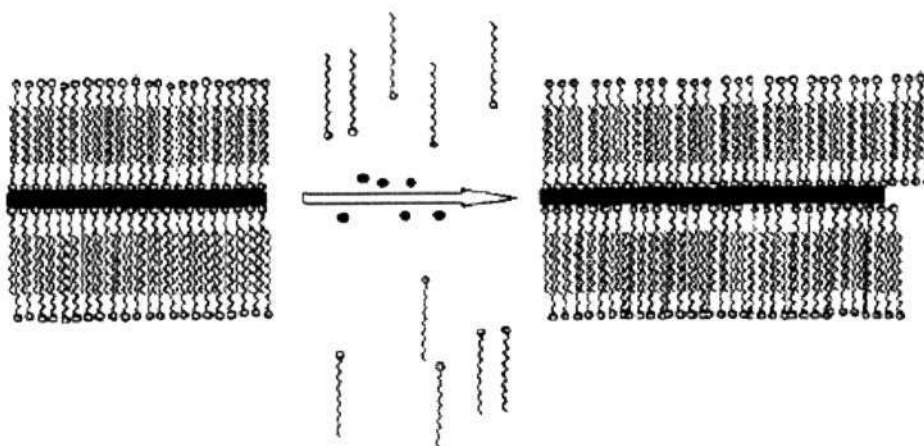
Figure 1.8 bilayer of CTAB (squiggles) on the gold nanorod (black rectangle) surface [Ref.66].

It has been demonstrated that some approaches are available for controlled assembly of GNRs [67]. For example, interactions between deoxyribonucleic acid (DNA) and its complementary strand have been used to assemble gold nanowires on a solid surface [68] or in solution [69]. Gold nanorods have been linked to form 1-D chains using various linker molecules such as 3-mercaptopropionic acid, cysteine, Glutathione, alkanedithiols, biotin–streptavidin connectors etc [70-74]. Figure 1.9 shows the TEM image of the chains of gold nanorods formed by the interaction with cysteine and the corresponding change in the UV-visible spectra. As the nanorods are linked to form chains the longitudinal surface plasmon band shifts to longer wavelengths as shown in Figure [67].
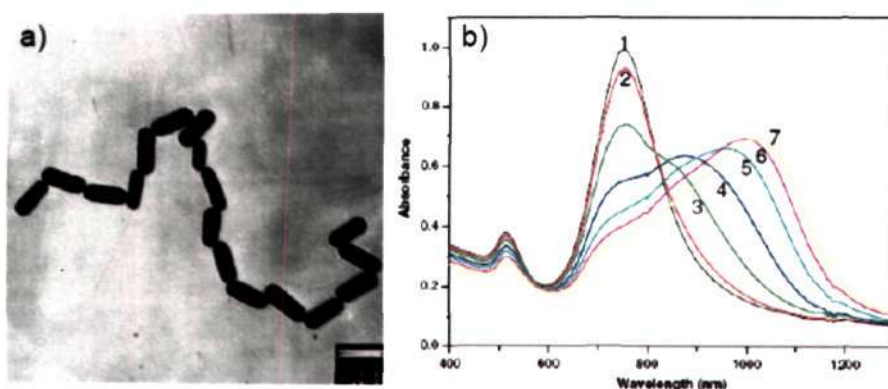
Figure 1.9 (a) TEM images and (b) of chains of gold nanorods in the presence of cysteine [Ref.67].

1.3 Nanocrystalline film at Liquid-liquid interface

Ultrathin films of metal nanocrystals constitute a novel class of materials with a unique combination of nominally zero and two dimensionalities. Interfaces are an important means to generate two-dimensional self assemblies of nanocrystals, providing a constrained environment for organized assembly. The air–water interface has been exploited for the preparation of films of metals and semiconductors, which have potential applications in nanodevices. For example, Chi et al. [75] have reported the preparation of

monolayers of Au_{55} nanocrystals by spreading its chloroform sol over the aqueous layer in an LB trough and then transferring it onto a substrate. Large-scale ordered arrays of such nanocrystals have been obtained by Brown et al [76]. Sastry and co-workers synthesized hydrophobically modified Au nanoparticles and organized them into lamellar films by the LB method [77]. Properties of thin films obtained by the LB technique are determined by the nature of the substrate as well as the reaction conditions, and the films are generally polycrystalline.

Unlike the air–water interface, the liquid–liquid (organic-aqueous) interface has not been investigated sufficiently. Nanocrystalline films can be prepared by a simple one-step synthesis at the liquid-liquid interface wherein an organometallic compound dissolved in an organic layer reacts with the reducing agent present in the aqueous layer at the interface as shown in Figure 1.10 [78]. A careful examination has shown that the material formed at the interface is an ultrathin nanocrystalline film consisting of closely packed metal nanocrystals coated with the organic species present at the interface [79]. The film at the interface is essentially freestanding and can be deposited onto a substrate for further investigation or could be converted to either an organosol or a hydrosol by using appropriate capping agents [79, 80].
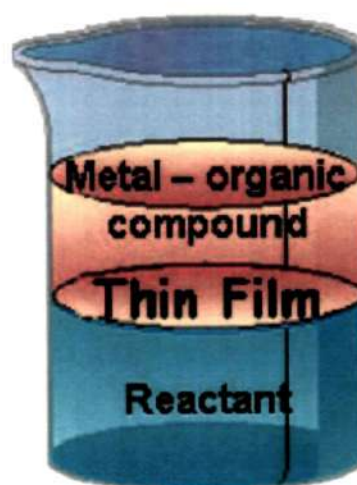
Figure 1.10 Schematic showing the formation of film at liquid-liquid interface [Ref.78].

Figure 1.11 shows nanocrystalline film of Au formed at the toluene-water interface by the reaction of Au(PPh$_3$)Cl in toluene and alkaline solution of tetrakis(hydroxmethyl) phosphoniumchloride (THPC) in water. With the addition of a few micromoles of capping agents such as dodecanethiol or octylamine to the toluene layer, the Au film at the interface disappeared within minutes, accompanied by a distinctive pink coloration in the top layer as shown in Figure 1.11 (Left) that is characteristic of an Au organosol. Similarly, the addition of a few micromoles of mercaptoundecanoic acid (MUA) to the aqueous solution results in the complete dissolution of the film after a few hours and the transfer of its contents to the aqueous layer as in Figure 1.11 (Right) [80].

Figure 1.11 Nanocrystalline film of Au formed at the toluene-water interface (middle). When dodecanethiol is added to the toluene layer, the film breaks up forming an organosol(left) while mercaptoundecanoic acid added to water it produces a hydrosol (right) [Ref.80].

Figure 1.12 shows the optical spectrum and corresponding TEM images of the nanocrystalline film and the changes on perturbation through sonication or interaction

with an alkanethiol [81]. The spectrum corresponding to a nanocrystalline film obtained

at the liquid-liquid interface at room temperature exhibits a broad band centered at 700

nm, with a weak shoulder at around 540 nm. While the absorption band around 540 nm is

characteristic of surface plasmons from uncoupled nanocrystals, the higher wavelength

band at 700nm is a typical response from an assembly of interacting nanocrystals [82].

As evident from the corresponding TEM image (Figure 1.12), the nanocrystalline film

consists of close-packed assembly of particles with ~1 nm spacing due to the organic

shell. The collective absorption is affected when the nanocrystalline film is subjected to

ultrasonication as can be seen in spectrum 'b' of Figure 1.12. There is a rise in absorption

at 540 nm followed by an ill-defined broad feature. With the addition of alkanethiol a

well-defined band around 530 nm (spectrum c of Figure 1.12) is obtained, typical of

uncoupled colloidal gold nanocrystals. Accordingly, the TEM image shows isolated

nanocrystals.
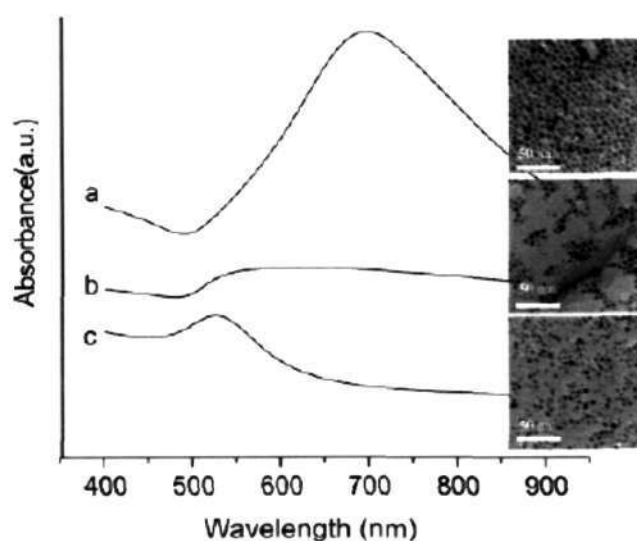
Figure 1.12 Optical absorption spectra of (a) an Au nanocrystalline film prepared at
the liquid-liquid interface and deposited on a glass substrate, (b) a sol obtained by
sonicating the film in toluene for 3 min, (c) a sol obtained by derivatizing the
nanocrystals from the film using hexadecanethiol in toluene. The corresponding
TEM images are shown [Ref.81].

1.4 Growth of nanocrystals

For the fabrication of nanoparticles, a small size is not the only requirement. For any practical application, the processing conditions need to be controlled in such a way that resulting nanoparticles have the following characteristics: (i) identical size of all particles, (ii) identical shape or morphology, (iii) identical chemical composition and crystal structure and (iv) individually dispersed [18]. Better understanding of the growth mechanism and careful control of the growth parameters are required to meet these characteristics.

In solution when the concentration of the growth species increases above the equilibrium concentration, initially there will be no nucleation. Nucleation occurs when the concentration reaches the minimum saturation required to overcome the critical energy barrier, and the nucleation rate increases very rapidly as the concentration increases further. Once nuclei are formed, growth occurs simultaneously. Above the minimum concentration, nucleation and growth are inseparable processes; however, these two processes proceed at different speeds. When the concentration decreases below this specific concentration, which corresponds to the critical energy, no more nuclei would form, whereas the growth will proceed until the concentration of growth species has attained the equilibrium concentration or solubility (see Figure 1.12) [83].
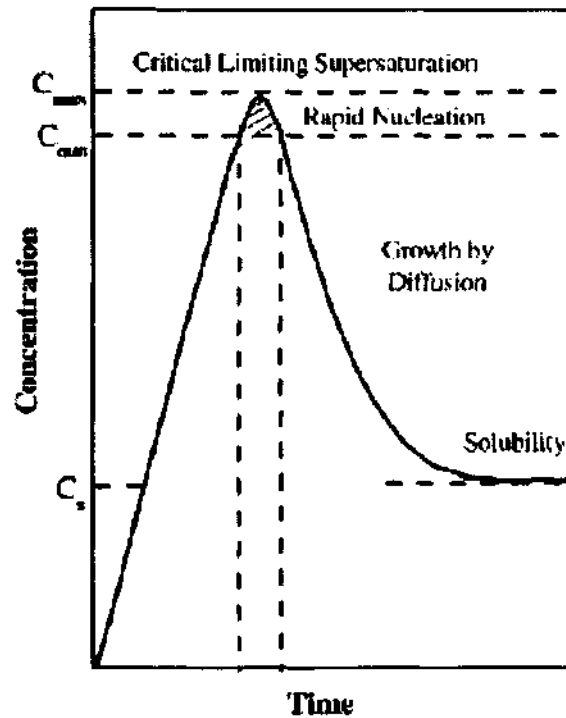
Figure 1.13 Schematic illustrating the processes of nucleation and subsequent growth [Ref.83].

There are various mechanisms by which particles grow in solution [83]. As a result of the large surface area present for small particles, surface excess energy becomes more important in very small particles, constituting a non-negligible percentage of the total energy. Hence, for a solution that is initially not in thermodynamic equilibrium, a mechanism that allows the formation of larger particles at the cost of smaller particles reduces the surface energy and hence plays a key role in the growth of nanocrystals. A colloidal particle grows by a sequence of monomer diffusion towards the surface followed by reaction of the monomers at the surface of the nanocrystal. Coarsening effects, controlled either by mass transport or diffusion, are often termed the Ostwald ripening process. This diffusion limited Ostwald ripening process is the most

predominant growth mechanism and was first quantified by Lifshitz and Slyozov [84], followed by a related work by Wagner [85], known as the LSW theory.

The diffusion process is dominated by the surface energy of the nanoparticle. The interfacial energy is the energy associated with an interface due to differences between the chemical potential of atoms in an interfacial region and atoms in neighboring bulk phases. For a solid species present at a solid/liquid interface, the chemical potential of a particle increases with decreasing particle size, the equilibrium solute concentration for a small particle is much higher than for a large particle, as described by the Gibbs–Thompson equation. The resulting concentration gradients lead to transport of the solute from the small particles to the larger particles. The equilibrium concentration of the nanocrystal in the liquid phase is dependent on the local curvature of the solid phase. Differences in the local equilibrium concentrations, due to variations in curvature, set up concentration gradients and provide the driving force for the growth of larger particles at the expense of smaller particles [86]. In case of Ostwald ripening the dependence of the particle size on time is given by

$$D^3 - D^3{}_0 = Kt$$

Where D and D_0 are the average particle diameter at time t and at time t=0 respectively. The rate const K is given by $K = 8\gamma d V_m{}^2 C_\infty / 9RT$, where d is the diffusion constant at temperature T, V_m the molar volume, γ the surface energy, and C_∞ the equilibrium concentration at a flat surface.

Besides the diffusion process, another important process in the growth of any particle is the reaction at the surface where the units of diffusing particles are assimilated into the growing nanocrystal. When the diffusion of growth species from the bulk to the

growth surface is sufficiently rapid the growth rate is controlled by the surface process. In that case the growth rate is limited by the surface reaction of the monomers and the rate law would be given by

$$D^2 \propto t$$

While in the preceding two sections, we have discussed the two limiting cases, in practice it is to be expected that both diffusion and surface reaction will contribute to the growth process in real experimental conditions. Specifically, several recent reports [87, 88] have stressed that the growth in a variety of realistic systems does not belong to either of the two limits, namely the diffusion or the reaction-limited regimes, but is controlled by a combination of diffusion and reaction at the surface

$$BD^3 + CD^2 + const = t$$

where, $B = AT/\exp(-E_a/k_B T)$, $A \propto 1/(D_0 \gamma V_m^2 C_\infty)$ and $C \propto T/(k_d \gamma V_m^2 C_\infty)$, k_d is the rate constant of surface reaction.

For better understanding of the growth mechanism of nanocrystals in solution thorough studies using techniques such as Small Angle X-Ray Scattering (SAXS), transmission electron microscopy (TEM), optical spectroscopy, etc. are required.

References

1. H. Zhao, Y. Ning, Gold Bull., **2000**, *33*, 103.

2. M. Faraday, Philos. Trans. R. Soc. London., **1857**, *147*, 145.

3. M. A. El-Sayed, Acc. Chem. Res., **2001**, *34*, 257.

4. U. Kreibig, M. Vollmer, Springer: Berlin, **1995**.

5. G. C. Papavassiliou, Prog. Solid State Chem., **1979**, *12*, 185.

6. K. L. Kelly, E. Coronado, L. L. Zhao, G. C. Schatz, J. Phys. Chem. B, **2003**, *107*, **668**.

7. S. Link, M. A. El-Sayed, Int. Rev. Phy. Chem., **2000**, *19*, 409.

8. G. Mie, Ann. Phys., **1908**, *25*, 329.

9. J. A. Creighton, D. G Eadon, J. Chem. Soc., Faraday Trans., **1991**, *87*, 3881.

10. P. Mulvaney, Langmuir, **1996**, *12*, 788.

11. H. Hirai, H. Wakabayashi, M. Komiyama, Chem. Lett., **1983**, 1047.

12. P.-A. Brugger, P. Cuendet, M. Gratzel, J. Am. Chem. Soc., **1981**, *103*, 2923.

13. J. M. Thomas, Pure Appl. Chem., **1988**, *60*, 1517.

14. R. Gans, Ann. Phys., **1915**, *47*, 270.

15. S. Link, M. A. El-Sayed, J. Phys. Chem. B, **1999**, *103*, 8410.

16. F. Kim, J. H. Song, P. Yang, J. Am. Chem. Soc., **2002**, *124*, 14316.

17. G. T. Boyd, Z. H. Yu, Y. R. Shen, Phys. Rev. B, **1986**, *33*, 7923.

18. G. Cao, Nanostructures & Nanomaterials: Synthesis, Properties & Applications, Imperial College Press, London, **2004**.

19. C. B. Murray, C. R. Kagan, M. G. Bawendi, Ann. Rev. Mater. Sci., **2000**, *30*, 545.

20. A. J. Sutherland. Curr. Opn. Sol. Stat. Mater. Sci., **2002**, *6*, 365.

21. M. Nirmal, L. Brus. Acc. Chem. Res., **1999**, *32*, 407.

22. Y. Huang, X. F. Duan, Q. Q. Wei, C. M. Lieber, Science, **2001**, *291*, 630.N

23. I. W. Hamley, Angew. Chem. Int. Ed., **2003**, *42*, 1692.

24. A. P. Alivisatos, K. P. Johnsson, X. G. Peng, T. E. Wilson, C. J. Loweth, M. P. Bruchez, P. G. Schultz, Nature, **1996**, *382*, 609.

25. P. C. Ohara, J. R. Heath, W. M. Gelbart, Angew. Chem. Int. Ed., **1997**, *36*, 1078.

26. B. A. Korgel, D. Fitzmaurice, Adv. Mater., **1998**, *10*, 661.

27. M. Li, H. Schnablegger, S. Mann, Nature, **1999**, *402*, 393.40

28. T. L. Breen, J. Tien, S. R. J. Oliver, T. Hadzic, G. M. Whitesides, Science, **1999**, *284*, 948.

29. A. N. Shipway, E. Katz, I. Willner, Chem. Phys. Chem, **2000**, *1*, 18.

30. Q. Dai, J. G. Worden, J. Trullinger, Q. Huo, J. Am. Chem. Soc., **2005**, *127*, 8008.

31. Y. Kang, K. J. Erickson, T. A. Taton, J. Am. Chem. Soc., **2005**, 127, 13800.

32. H. Fan, E. Leve, J. Gabaldon, A. Wright, R. E. Haddad, C. J. Brinker, Adv. Mater., **2005**, *17*, 2587.

33. J. Huang, F. Kim, A. R. Tao, S. Connor, P. Yang, Nat. Mater., **2005**, *4*, 896.

34. M. Wanunu, R. P. Biro, H. Cohen, A. Vaskevich, I. Rubinstein, J. Am. Chem. Soc., **2005**, *127*, 9207.

35. D. S. Sidhaye, S. Kashyap, M. Sastry, S. Hotha, B. L. V. Prasad, Langmuir, **2005**, *21*, 7979.

36. S. Huang, H. Ma, X. Zhang, F. Yong, X. Feng, W. Pan, X. Wang, Y. Wang, S. Chen, J. Phys. Chem. B, **2005**, *109*, 19823.

References

37. S. A. Claridge, S. L. Goh, J. M. J. Frechet, S. C. Williams, C. M. Micheel, A. P. Alivisatos, Chem. Mater., 2005, *17*, 1628.

38. N. C. Harris, C-H. Kiang, Phys. Rev. Lett., 2005, *95*, 046101.

39. V. Germain, M-P. Pileni, Adv. Mater., 2005, *17*, 1424.

40. J. H. Warner, R. D. Tilley, Adv. Mater., 2005, *17*, 2997.

41. B. Liu, H. C. Zeng, J. Am. Chem. Soc., 2005, *127*, 18262.

42. C. N. R. Rao, A. Govindaraj, S. R. C. Vivekchand, Annu. Rep. Prog. Chem., Sect. A: Inorg. Chem., 2006, *102*, 20.

43. B. Nikoobakht, Z. L. Wang, M. A. El-Sayed, J. Phys. Chem. B, 2000, *104*, 8635.

44. N. R. Jana, L. A. Gearheart, S. A. Obare, C. J. Johnson, K. J. Edler, S. Mann, C. J. Murphy, J. Mater. Chem., 2002, *12*, 2909.

45. N. R. Jana, Chem. Commun., 2003, *15*, 1950.

46. N. R. Jana, Angew. Chem., 2004, *116*, 1562.

47. C. J. Orendorff, P. L. Hankins, C. J. Murphy, Langmuir, 2005, *21*, 2022.

48. S-W. Chung, G. Markovich, J. R. Heath, J. Phys. Chem. B, 1998, *102*, 6685.

49. B. Nikoobakth, Z. L. Wang, M. A. El-Sayed, J. Phys. Chem.B, 2000, *104*, 8635.

50. E. Dujardin, L.-B. Hsin, C. R. C. Wang, S. Mann, Chem. Commun., 2001, 1264

51. C. A. Mirkin, R. L. Letsinger, R. C. Mucic, J. J. Storhoff, Nature, 1996, *382*, 607.

52. C. M. Niemeyer, W. Burger, J. Peplies, Angew. Chem., Int. Ed., 1998, *37*, 2265.

53. J. J. Storhoff, C. A. Mirkin, Chem. Rev., 1999, *99*, 1849.

54. C. B. W. Garcia, Y. Zhang, S. Mahajan, F. DiSalvo, U. Wiesner, J. Am. Chem. Soc., 2003, *125*, 13310.

55. A. D. Ormonde, E. C. M. Hicks, J. Castillo, R. P. Van Duyne, Langmuir, **2004**, *20*, 6927.

56. H. Lee, A. M. Purdon, V. Chu, R. M. Westervelt, Nano. Lett., **2004**, *4*, 995.

57. C. J. Orendorff, A. Gole, T. K. Sau, C. J. Murphy, Anal. Chem., **2005**, *77*, 3261.

58. C. J. Murphy, T. K. Sau, A. M. Gole, C. J. Orendorff, J .X. Gao, L. F. Gou, S. E. Hunyadi, T. Li, J. Phys. Chem. B, **2005**, *109*, 13857.

59. C. Z Li, K. B. Male, S. Hrapovic, J. H. T. Luong, Chem. Commun., **2005**, *31*, 3924.

60. B. Nikoobakht, Z. L. Wang, M. A. El-Sayed, J. Phys. Chem. B, **2000**, *104*, 8635.

61. A. Gole, C. J. Orendorff, C. J. Murphy, Langmuir, **2004**, *20*, 7117.

62. A. Gole, C. J. Murphy, Chem. Mater. **2005**, *17*, 1325.

63. Z.L. Wang, M.B. Mohamed, S. Link, M.A. El-Sayed, Surface Science, **1999**, *440*, L809.

64. B. Nikoobakht, M. A. El-Sayed, Langmuir, **2001**, *17*, 6368.

65. C. J Johnson, E. Dujardin, S. A. Davis, C. J. Murphy, S. Mann, J. Mater. Chem., 2002, 12, 1765.

66. J. Gao, C. M. Bender, C. J. Murphy, Langmuir, **2003**, *19*, 9065.

67. X. Hu, W. Cheng, T. Wang, E. Wang, S. Dong, Nanotechnology, **2005**, *16*, 2164.

68. J. N. K. Mbindyo, B. D. Reiss, B. R. Martin, C. D. Keating, M. J. Natan, T. E. Mallouk, Adv. Mater. **2001**, *13*, 249.

69. E. Dujardin, L-B. Hsin, C. R. C. Wang, S. Mann, Chem. Commun., **2001**, *14*, 1264.

70. K. G. Thomas, S. Barazzouk, B. I. Ipe, S. T. S. Joseph, P. V. Kamat, J. Phys. Chem. B, **2004**, *108*, 13066.

71. S. Zhang, X. Kou, Z. Yang, Q. Shi, G. D. Stucky, L. Sun, J. Wang, C. Yan, Chem. Commun., **2007**, 1816.

72. P. K. Sudeep, S. T. S Joseph, K. G Thomas, J. Am. Chem. Soc., **2005**, *127*, 6516.

73. S. T. S. Joseph, B. I. Ipe, P. Pramod, K. G. Thomas, J. Phys. Chem. B, **2006**, *110*, 150.

74. K. K. Caswell, J. N. Wilson, U. H. F. Bunz, C. J. Murphy, J. Am. Chem. Soc., **2003**, *125*, 13914.

75. L. F. Chi, S. Rakers, M. Hartig, H. Fuchs, G. Schmid, Thin Solid Films, **1998**, *327*, 520.

76. J. J. Brown, J. A. Porter, C. P. Daghlian, U. J. Gibson, Langmuir, **2001**, *17*, 7966.

77. M. Sastry, A. Gole, V. Patil, Thin Solid Films, **2001**, *384*, 125.

78. C. N. R. Rao, K. P. Kalyanikutty, Acc. Chem. Res., **2008**, *41*, 489.

79. C. N. R Rao, G. U Kulkarni, P. J Thomas, V. V Agrawal, P. J Saravanan, Phys. Chem. B. **2003**, *107*, 7391.

80. V. V Agrawal, G. U. Kulkarni, C. N. R. Rao, J. Phys. Chem. B, **2005**, *109*, 7300.

81. V. V. Agrawal, N. Varghese, G. U. Kulkarni, C. N. R. Rao, Langmuir, **2008**, *24*, 2494.

82. L. Gunnarsson, T. Rindzevicius, J. Prikulis, B. Kasemo, M. Kall, S. Zou, G. C. Schatz, J. Phys. Chem. B, **2005**, *109*, 1079.

83. C. N. R. Rao, A. Muller, A. K. Cheetham (Eds.), Nanomaterials Chemistry: Recent Developments and New Directions, Wiley–VCH Verlag GmbH & Co., **2007**.

84. I. M. Lifshitz, V. V. Slyozov, J. Phys.Chem. Solids, **1961**, *19*, 35.

85. C. Wagner, Z. Elektrochem., **1961**, *65*, 581.

86. T. Sugimoto, Adv. Colloid Interface Sci., **1987**, *28*, 165.

87. D. V. Talapin, A. L. Rogach, M.Haase, H. Weller, J. Phys. Chem. B, **2001**, *105*, 12278.

88. R. Viswanatha, S. Sapra, B. Satpati,P. V. Satyam, B. N. Dev, D. D. Sarma, J. Mater. Chem., **2004**, *14*, 661.

Chapter 2

A calorimetric investigation of assembly, growth

and disassembly of nanomaterials

SUMMARY

Interaction of cysteine as well as 3-mercaptopropionic acid (MPA) with gold nanorods has been investigated with isothermal titration calorimetry (ITC), in combination with electronic absorption spectroscopy and transmission electron microscopy. The assembly process with MPA shows two steps, the first due to the binding of MPA to gold nanorods through the sulfur atom, and the second due to assembly of the MPA capped gold nanorods through the formation of cyclic hydrogen bonded dimers between the MPA molecules. In the case of cysteine only a single step is observed in ITC, due to the binding of sulfur to the gold rods.

The growth of gold nanocrystals has been investigated with ITC and the heat change associated with the growth is determined as ~10 kcalmol^{-1} per 1 nm increase in the nanocrystals diameter. Disintegration of gold nanofilms formed at the liquid-liquid interface by alkanethiols of different chain lengths has been monitored by calorimetry. The process involves two steps, the first step being the exothermic gold film-thiol interaction and the second step includes the endothermic disordering process followed by further thiol capping of isolated gold particles. The rate of interaction of the thiols with the film decreases with decreasing chain length.

Introduction

Calorimetry is the principal source of thermodynamic information. It is a very sensitive and general technique due to the fact that practically all physical, chemical and biological processes are accompanied by heat exchanges. Hence, calorimetry has become a powerful tool for expanding knowledge and understanding in many fields of science and technology. Isothermal titration calorimetry (ITC) is a calorimetric technique, which can measure the energetics of biochemical or molecular interactions at a constant temperature [1-4]. It is an ultrasensitive technique which can monitor precise changes in heat for a chemical reaction and resolve the binding stoichiometry, binding heat, and binding constant in one experiment. In determining these thermodynamic parameters, one compound in solution is generally added in small increments to a solution containing its binding partner, and the heat change is measured for each addition of the compound solution [2]. Determination of accurate thermodynamic parameters from such ITC data requires that the experimental isotherms be modeled in terms of the chemical processes that occur upon mixing the two solutions, taking into account how each process contributes to the measured heat. Owing to these unique strengths, ITC has been widely used to quantify various interactions.

ITC has been used to study various interactions such as Conformational transitions in macromolecules, Protein-ligand binding [4], Nucleic acid recognition, Enzyme kinetics [5], Drug design [6], Structure-energy correlations, Investigation of micelles [7] etc [8, 9]. We were interested to use ITC to study various interactions of

nanoparticles. There have been few studies which use ITC as a tool to study nanomaterials interactions. For example, Sastry et al. studied the binding of DNA bases and PNA base monomers to Gold nanoparticles using ITC [10]. Rao et al. used ITC to calculate and compare the interaction energy of various nucleobases with single walled carbon nanotubes [11]. In the present study we used isothermal titration calorimetry to monitor the heat change associated with various processes such as assembly of gold nanorods, growth of gold nanoparticles and disintegration of gold nanofilm at the liquid-liquid interface by various alkanethiols.

2.1 Scope of the present investigations

2.1.1 Assembly of gold nanorods

Self-assembly of nanostructures constitutes an important aspect in nanoscience and nanotechnology and several chemical strategies have been employed to create assemblies of nanoparticles [12, 13]. Gold nanorods have been assembled using DNA, surfactants and various linker molecules [14-20]. Linking has major consequences on the electronic spectra of the nanorods [16]. Thus when gold nanoparticles are packed closely to form a film, the surface plasmon resonance band of the gold film shifts progressively to longer wavelengths depends on the interparticle separation [21]. Gold nanorods exhibit another unique feature in the electronic spectra, in that they show transverse and longitudinal surface plasmon absorption bands [22]. The transverse band does not vary with the aspect ratio of the nanorods while the longitudinal plasmon band shifts to longer wavelength with increase in aspect ratio. Accordingly, on linking gold nanorods by mercaptopropionic acid (MPA) or cysteine to give rise to chains or necklaces, the

longitudinal surface plasmon resonance band shifts significantly to longer wavelengths [16,17].

Formation of chains and necklaces of gold nanorods using organic linker molecules would involve two processes: (1) interaction of the linker molecules with the gold nanorods and (2) formation of the extended chains or necklaces. When a thiolcarboxylic acid (MPA) and cysteine are used as linkers, the first process involves the formation of the metal-sulfur bond which is an exothermic reaction. The formation of necklaces would also involve an exothermic process. We have investigated the process of assembly of gold nanorods to form necklaces by isothermal titration calorimetry in combination with spectroscopic and transmission electron microscopic studies. For this purpose, we have employed 3-mercapatopropionic acid as the linker molecule wherein the linkage occurs through the formation of six-membered dimeric hydrogen bonded rings between the carboxylic groups [16] and also cysteine where electrostatic interactions lead to the assembly [17] as shown in scheme 1.

For cysteine
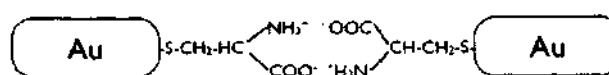
For MPA
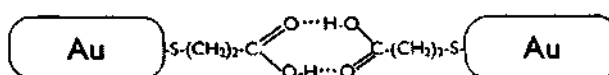
Scheme 1

2.1.2 Growth of gold nanocrystals

Nanomaterials show various shape dependent physical and chemical properties which has motivated intense research in this area [23]. Synthesis and processing of nanomaterials and nanostructures are the essential aspect of nanotechnology. Studies on

new physical properties and applications of nanomaterials and nanostructures are possible only when nanostructured materials are made available with desired size, morphology, crystal and microstructure and chemical composition [24]. The growing demand to obtain such nanocrystals is met largely by the solution route synthesis of nanocrystals [25, 26], due to its ease of implementation and high degree of flexibility. But the dependences of the average size and the size distribution of the generated particles on parameters of the reaction are not understood in detail and therefore, the optimal reaction conditions are arrived at essentially in an empirical and intuitive manner [27]. The understanding of coarsening processes that lead to growth of the minority phase within a majority phase by combining smaller particles is important both scientifically and for technological considerations [28, 29]. The kinetics of the growth of a solid from a solution, which is the most popular chemical method to produce a wide variety of systems with dimensions in the nanometer region, has been less investigated [30–33].

Several techniques have been used to study the kinetics of growth of nanocrystals to obtain an understanding of the mechanism by which the particles grow in solution. The most widely used techniques to follow growth are transmission electron microscopy (TEM), UV-visible spectroscopy, photoluminescence spectroscopy and small angle X-ray scattering (SAXS). We have monitored the growth of gold nanocrystals using isothermal titration calorimetry by the measuring the heat change associated with the process since there are hardly any which follow such growth calorimetrically [34, 35].

2.1.3 Disintegration of Gold nanofilms by alkanethiols

Mesoscalar assemblies of metal nanocrystals are of considerable interest since both short and long range interactions coexist in these systems and compete to give rise
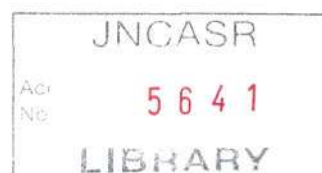
to a host of interesting structural, optical, electrical, magnetic and other properties [36-43]. A number of studies have aimed to explore their potential in technological applications [44-48]. A nanocrystal assembly, analogous to an atomic lattice, derives its properties from the nature of the nanocrystal (also called a superatom [49]), from its geometric arrangement, and from the nature of the material in the intervening space. Specifically in the case of a simple two dimensional hexagonal assembly, the main variables are the nanocrystal diameter, the interparticle separation, and the nature of the spacer molecule as well as the domain size. There are several reports on the synthesis of well-defined two-dimensional assemblies formed by suitably derivatizing the nanocrystals [50], by assembling at the air-water interface [51, 52], or by growing nanocrystals in predefined locations [53, 54]. These methods have enabled a greater degree of control on the structural and physical properties of nanocrystal assemblies.

We have been interested in investigating the disintegration process of metal nanocrystal assemblies caused by a variation in the interparticle distance. For this purpose, we have prepared nanocrystalline gold films at the liquid-liquid interface [55]. Unlike the literature procedures that involve at least two steps, this is a simple one-step synthesis, wherein an organometallic compound dissolved in an organic layer reacts with a reducing agent present in the aqueous layer at the interface. The film formed at the interface is an ultrathin nanocrystalline film consisting of closely packed metal nanocrystals, a few nanometers in diameter [56]. The film at the interface can be transferred to a toluene layer as an organosol by the addition of small amounts of alkanethiols. In the present study, we have investigated how heat changes associated with the disintegration process reflects the effects of changing interparticle separation between

the gold nanocrystals when the film interacts with alkanethiols of different chain lengths, $CH_3(CH_2)_nSH$. The study not only provides an insight into the collective behavior of the nanocrystals in the film and its dependence on the interparticle distance but also throws light on the nature of interaction of alkanethiols with metal nanoparticle assemblies. Thus, we find that the interaction between the nanoparticles decreases linearly with the increase in the separation between the nanoparticles as determined by the length of the alkane chain.

2.2 Experimental section

Isothermal titration calorimetry (ITC)

In ITC, the experiment is performed at a constant temperature [2]. A schematic diagram of a standard ITC instrument is shown in Figure 2.1. The instrument consists of two identical cells (volume typically 0.5 – 1.5 ml) housed in an isothermal jacket. These two cells are kept at thermal equilibrium ($\Delta T = 0$, see Figure 2.1) throughout the experiment. One cell is filled with water (for experiments performed in aqueous solvents) or buffer solution, and acts purely as a reference. The other (the sample cell) is filled with one component of the interaction to be investigated. Prior to use, solutions are degassed under vacuum (140 mbar, 8 min) to eliminate air bubbles. The basis of the experiment is to measure the heat energy per unit time (expressed in μW) that must be added to the sample cell to maintain zero temperature difference between the two cells at the designated temperature for an experiment.
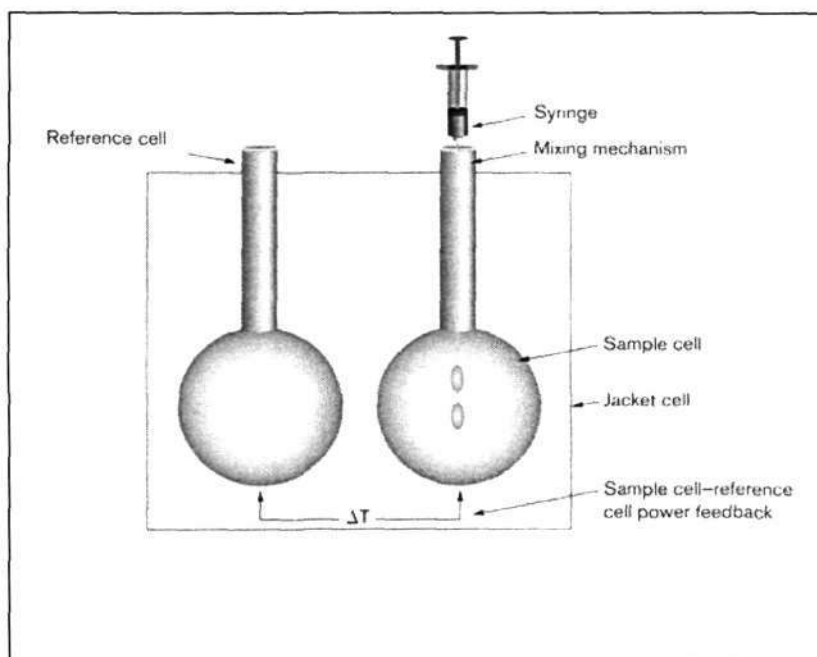
Figure 2.1 A schematic diagram of ITC instrument

When the second component is introduced in a series of aliquots (typically injections of 5-25 µl to give a total added volume of 50-250 µl) to the sample cell, an enthalpic change results. If the interaction is exothermic, less heat per unit time will be required by the sample cell to keep the two cells in thermal equilibrium; if the interaction is endothermic, the opposite effect will be observed. ITC uses a cell feedback network (CFB) to differentially measure and compensate for heat produced or absorbed between the sample and reference cell. The cells are in contact with thermopile/thermocouple circuits regulated by an interactive feedback control system, so the highly sensitive response to fluctuations in temperature between the cells and between the jacket and the cells can be detected. After each addition, the heat released or absorbed as a result of the reaction is monitored by the isothermal titration calorimeter as a peak of power against time for each injection. Addition of the second component is automated and occurs from a precision syringe driven by a computer-controlled stepper motor. The contents of the

sample cell are stirred to effect rapid mixing of the reactants. Mixing of the interacting

species, by stirring or by diffusion after fast injection is very rapid and response times of

instruments to incremental heats are typically less than 10 s. The amount of titrand

required per experiment depends on the magnitude of the heat change. As the substrate in

the cell becomes saturated with ligands, the heat signal diminishes until only background

heat of dilution is observed.

ITC observations are plotted as the power in μcal/sec needed to maintain the

reference and the sample cell at an identical temperature as shown in figure 2.2. The raw

data for an experiment consists of a series of spikes of heat flow (power), with every

spike corresponding to a ligand injection. These heat flow spikes/pulses are integrated

with respect to time, giving the total heat effect per injection. The data is acquired by

computer software developed by MicroCal LLC.
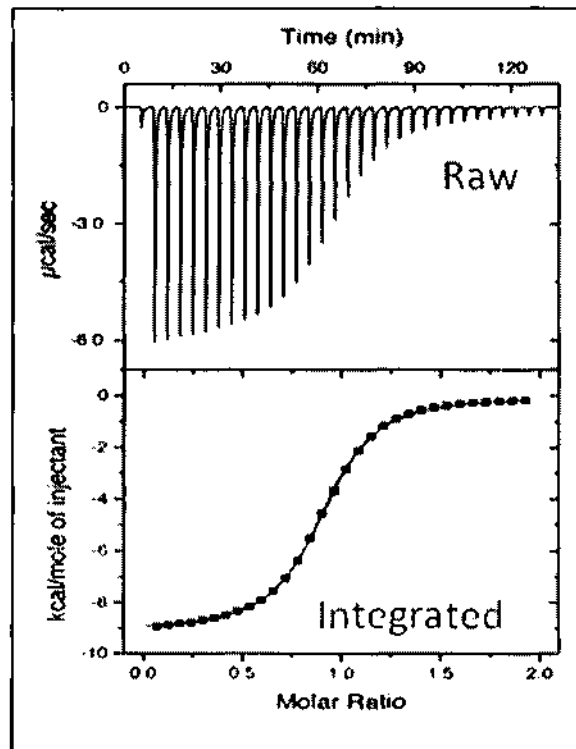
Figure 2.2 Raw data and integrated plot in ITC

2.2.1   Assembly of gold nanorods

Synthesis of and characterization gold nanorods

The gold nanorods were prepared using the photochemical method described in the literature [57]. In a typical preparation, 1.78 mg of tetraoctylammonium bromide was added to 6 mL 0.08 M aqueous solution of cetyl trimethylammonium bromide (CTAB), followed by the addition of 120 μL of 0.1 M hydrogen tetracholoaurate, 130 μL of acetone and 90 μL of cyclohexane. A small amount of silver nitrate solution (90 μL of 0.01 M) was added to the above mixture and the solution was taken in a quartz tube and irradiated with UV light for 14 hours. The resulting solution was blue in color and centrifuged at 7000 rpm for 15 minutes. The precipitate was collected, dispersed in distilled water and centrifuged at 7000 rpm twice. The resulting solution was used for the further experiments.

The prepared gold nanorods were characterized using UV-visible spectroscopy and transmission electron microscopy (TEM). All the UV-visible spectral experiments were performed using a Perkin-Elmer Lamda 900 UV/VIS/NIR spectrometer while the TEM images were recorded using JEOL JEM 3010 instrument fitted with a Gatan CCD camera at an accelerating voltage of 300 kV.

Monitoring the Assembly of nanorods by ITC

We have used mercaptopropionic acid (MPA) and cysteine as linkers to study the assembly process. The end to end assembly of nanorods can be followed by UV-vis

spectroscopy as the longitudinal plasmon band shifts to higher wavelengths with chain formation. We carried out the assembly of gold nanorods in isothermal titration calorimeter to monitor the heat changes associated with the assembly process. The UV-vis and TEM measurements were done after the experiments in ITC to confirm the chain formation. The calorimetric experimental details are as follows.

Isothermal titration calorimetric (ITC) experiments were performed using a Microcal VP-ITC instrument at 30°C [2]. In a typical titration, 2 μL of 0.57 mM solution of cysteine or MPA taken in the syringe were injected in equal intervals of 5 minutes to a solution of 1.59 nM solution of gold nanorods which was taken in the sample cell with 1.47 mL capacity. A total of 130 μL of cysteine or MPA was added to Au nanorod solution and the heat change to the first injection was not considered in the calculations [2]. The concentration of gold nanorods was calculated using the molar extinction coefficient of the surface plasmon resonance band of gold nanorods [58]. The reference cell of the microcalorimeter was filled with distilled water and both the cells were maintained at the same temperature. When cysteine/MPA is injected to the sample cell containing gold nanorods, the difference in heat needed to keep both the sample cell and reference cell at the same temperature is monitored. After the titration the samples were analyzed using UV-visible spectroscopy and transmission electron microscopy. Control experiments were carried out by titrating cysteine or MPA with distilled water under the same conditions and were subtracted with the experimental data to remove the dilution effects of the injectant.

2.2.2 Growth of gold nanocrystals

Gold sols were prepared following the method of Duff et al.[59] using alkaline solutions of THPC to reduce $HAuCl_4$. Typically, to 6.25 mL of aqueous 25 mM NaOH in a 50 mL beaker, 250 μL of THPC solution (480 μL of 80% THPC diluted to 10 ml) was added. After 5 min, 250 μL (0.006 mmol) of 50 mM $HAuCl_4$ was added rapidly while shaking the beaker. In order study the effect of concentration of $HAuCl_4$ on growth of the gold nanocrystals, we also carried out the reactions with higher concentration of $HAuCl_4$, i. e., 375 μL (0.018 mmol) of 50 mM solution. TEM studies were carried out with a JEOL (JEM3010) microscope operating at an accelerating voltage of 300 kV.

Isothermal titration calorimetric (ITC) experiments were performed as follows. As soon as the gold nanocrystals were formed in beaker, the hydrosol was filled in the sample cell of the calorimeter. The reference cell of the calorimeter was filled with distilled water and both the cells were maintained at the same temperature. 2 μL of distilled water taken in the syringe were injected in equal intervals of 5 minutes to the sample cell with 1.47 mL capacity to monitor the heat change during the growth process. Heat changes for the growth were measured over the 10 to 750 min range.

2.2.3 Disintegration of gold films by alkanethiols

In a typical experiment, the sample cell of the microcalorimeter was filled with 0.9 mL of 6.25 mM solution of NaOH and 37.5μL of 50mM solution of THPC. 0.85 mL of 1.5 mM solution of $Au(PPh_3)Cl$ in toluene was added to the cell and the solution

was kept undisturbed for 23 hours for the formation of the film. The reference cell was filled with 0.9 mL distilled water and 0.85 mL toluene and both cells were maintained at the same temperature. A syringe of 280μL capacity was filled with 1.73M solution of the alkanethiol. 5μL of 1.73M solution of alkanethiol taken in the syringe were injected in equal intervals of 5 minutes to the mixture (film) in the sample cell and the heat chanes for each injection was measured. Control experiments were carried out by the addition of same concentration of alkanethiol to a 0.9mL distilled water and 0.85mL toluene taken in the sample cell and subtracted with the experimental data to remove the dilution effects of alkanethiol.

2.3 Results and discussion

2.3.1 Assembly of gold nanorods

The as-prepared gold nanorods were characterized using UV-visible spectroscopy and transmission electron microscopy (TEM). The TEM images of the as prepared nanorods are shown in Figure 2.3a. All the nanorods were well separated as it is seen in the figure. The average length of the nanorods is 40nm and it average diameter is 18nm. UV-vis spectra show two bands due to surface plasmon resonance. The transverse surface plasmon band appeared around 520nm and longitudinal band was around 605nm as shown in Figure 2.3b.
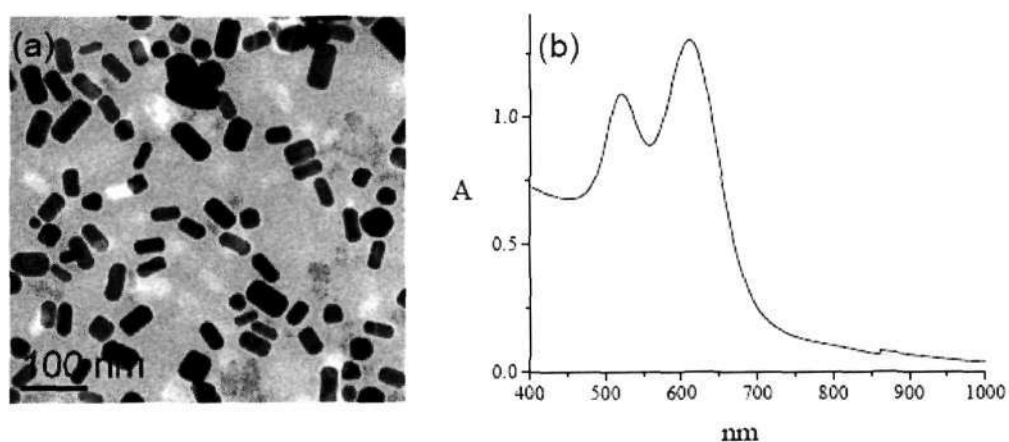
Figure 2.3 (a) TEM micrographs and (b) UV-visible spectra of gold nanorods

The additions of the linkers lead to the end to end assembly which is evidenced by UV-vis spectroscopy. Figure 2.4 shows the changes in optical spectra with time after the addition of mercaptopropionic acid to the as prepared gold nanorods. Each spectrum is recorded in the interval of 5min after the initial addition of MPA. As the nanorods are assembled to form chains the longitudinal band shifted to higher wavelengths.
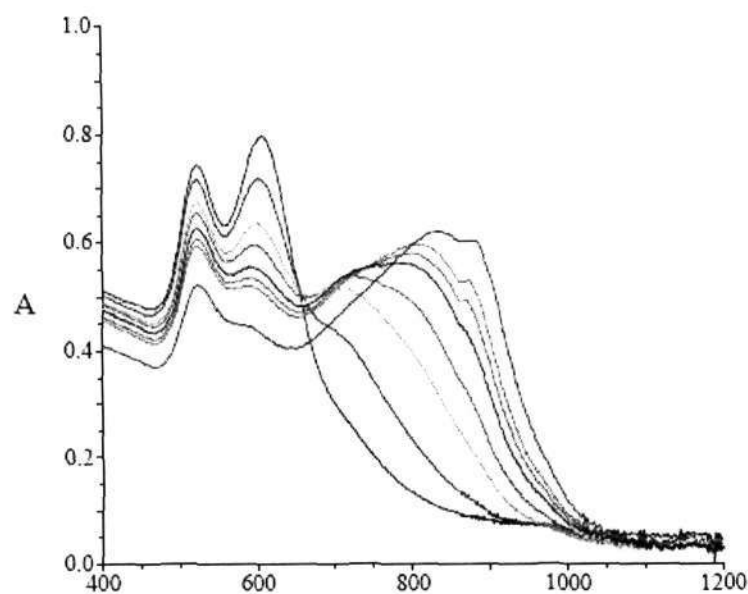
Figure 2.4 Change in UV-visible spectra of gold nanorods with addition of 3-mercaptopropionic acid

In ITC, we first carried out the study of the linking of gold nanorods to form necklaces by interactions with cysteine. The raw data obtained during the injections of cysteine to gold nanorods are shown in Figure 2.5a. At each injection, an exothermic reaction occurs. Figure 2.5(b) shows the integrated plot of the data in Figure 2.5a, achieved by integrating each peak and normalizing with respect to the concentration of cysteine added.
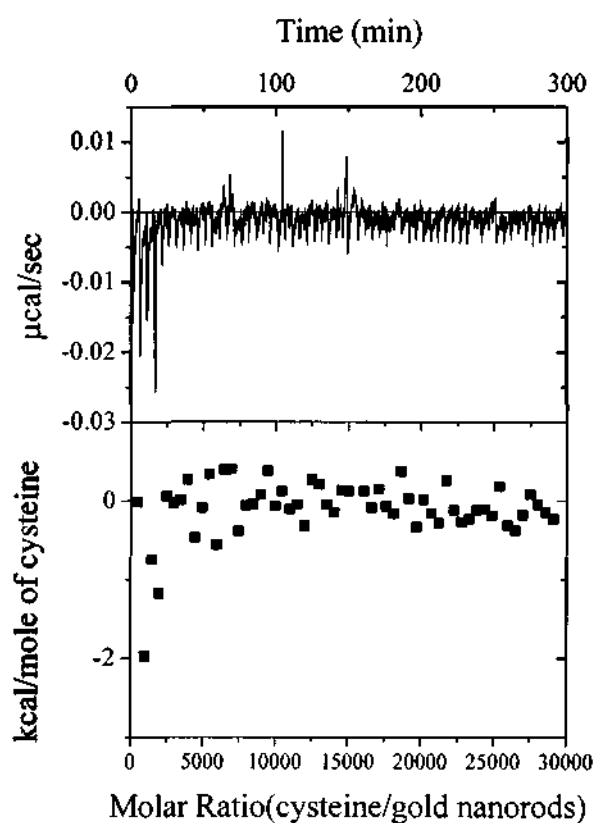
Figure 2.5 (a) Raw calorimetric data obtained by the titration of 0.57 mM cysteine with 1.59 nM gold nanorod solution and (b) binding isotherm plot obtained by integrating each peak in raw data and normalizing with cysteine concentration

The integrated plot gives the dependence of the heat exchange at each injection in kcal/mole of cysteine on the molar ratio of cysteine to that of gold nanorods. The data in Figure 2.5(b) were obtained after accounting for dilution effects. We observe that the

exothermicity of the peaks decreases from one injection to the next due to the binding of

cysteine molecules to the gold nanorods forming Au-S bonds. The number of free sites

available on the gold nanorods for the binding of cysteine decreases as the reaction

progresses, thereby reducing the exothermicity with progressive injections. The actual

formation of chains or necklaces of gold nanorods occurs by weak electrostatic

interaction of the cysteine molecules which cannot be detected by ITC [60]. We therefore

observe only a one step process corresponding to the binding of thiol to Au nanorods.

The process of assembly occurring through the interaction of the gold nanorods

with cysteine is directly evidenced in the electronic absorption spectra and transmission

electron microscopic images. Figure 2.6a shows how the electronic absorption spectra of

the as-prepared nanorods changes after the addition of cysteine.
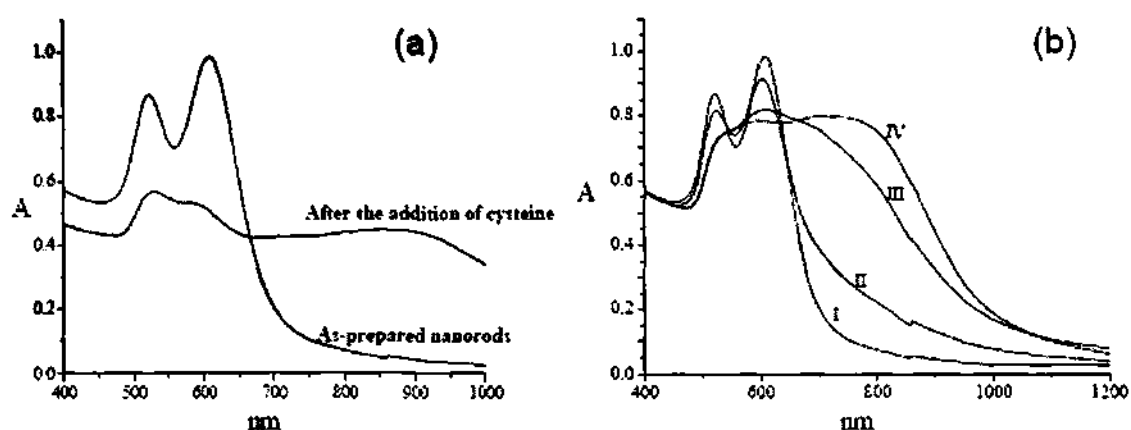
Figure 2.6 UV-visible spectra of gold nanorods (a) before and after calorimetric

titration with cysteine and (b) taken at different stages of the calorimetric titration

with MPA as indicated in Figure 8(b).

The nanorods show the transverse and longitudinal surface plasmon resonance

bands at 520 and 605 nm respectively [11] before the addition of cysteine. After the

addition of cysteine, the intensity of the longitudinal surface plasmon band decreases and a new broad band appears in the region 800-900 nm due to formation of chains or necklaces arising from the linking of the gold nanorods by the electrostatic interaction between cysteine molecules. The TEM image in Figure 2.7a shows the presence of randomly oriented Au nanorods in the as-prepared gold nanorods. The formation of necklaces of nanorods after the addition of cysteine is evidenced in the image shown in Figure 2.7b.
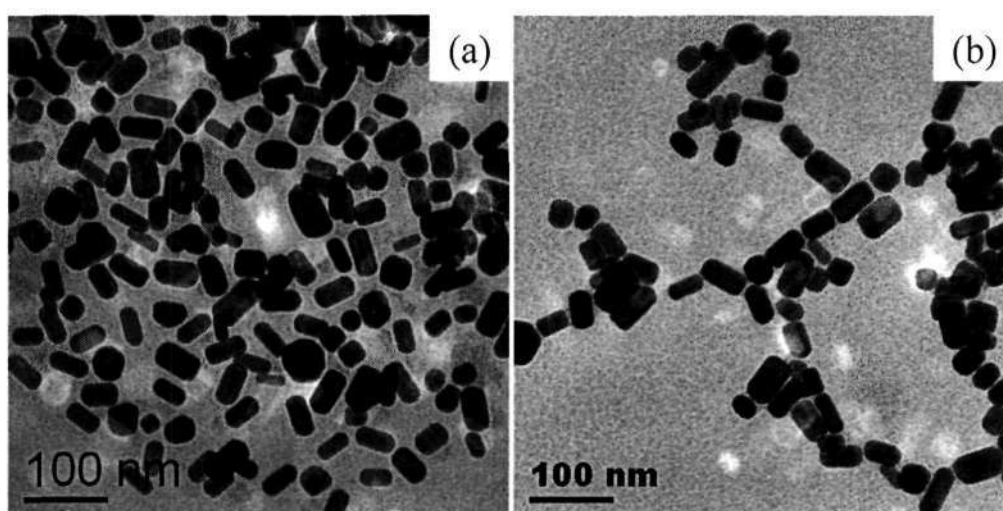
Figure 2.7 TEM micrographs of gold nanorods (a) before and (b) after calorimetric titration with cysteine.

The thermodynamics of interaction of cysteine molecules with the gold nanorods can be understood based on the calorimetric data obtained. Assuming that the energy released is due to the formation of Au-S bond only, since the energy associated with electrostatic interaction is negligible [47], the number of cysteine molecules bonded to each nanorod can be estimated. The binding of thiol to the gold nanorods involves the following reaction:

$$R\text{-}S\text{-}H + Au \rightarrow R\text{-}S\text{-}Au + \tfrac{1}{2}\,H_2$$
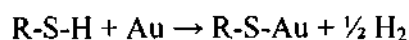
From the bond energies of RS-H, RS-Au, H-H bond which are 87 kcal/mole, 40 kcal/mole and 104 kcal/mole respectively, the net enthalpy of binding of thiol to Au is -5 kcal/mole [61]. The total heat liberated in the cysteine titration is -966 kcal per mole of Au nanorods. The average number of cysteine molecules attached to Au nanorods thus works out to be around 193.

The results of our calorimetric studies of the interaction of the thiol carboxylic acid, MPA, with gold nanorods are quite different from those with cysteine. In the case of MPA, we observe two steps in the calorimetric data as can be seen in Figure 2.8. To understand the binding process of MPA with the gold nanorods, we performed separate experiments wherein the reaction was stopped at different stages (after 12 and 22 injections) and the product analyzed using TEM and UV-visible spectroscopy. In Figure 2.6(b), we show the absorption spectra of Au nanorods taken at different stages

Figure 2.8 (a) Raw calorimetric data obtained by the titration of 0.57 mM 3-mercaptopropionic acid (MPA) with 1.59 nM gold nanorod solution and (b)binding isotherm plot obtained by integrating each peak in raw data and normalizing with MPA concentration.

during the binding process indicated in Figure 2.8(b). The longitudinal plasmon

resonance band does not shift after the first few injections of MPA (point II), and shows

significant shifts after 22 injections (point III). We assign the first step in the calorimetric

data to the binding of MPA molecules to Au nanorods or the formation of Au-S bonds.

The second step corresponds to the binding of gold nanorods to form chains or necklaces

through the formation of six-membered cyclic hydrogen bonded units between the

carboxylic acid groups of MPA. In Figure 2.9, we show the TEM image of the as

prepared gold nanorods and the necklaces formed by the nanorods after the addition of

MPA. Such an occurrence of two steps has been noted in the dynamics of gold nanorod-

alkanedithiol interaction [19].
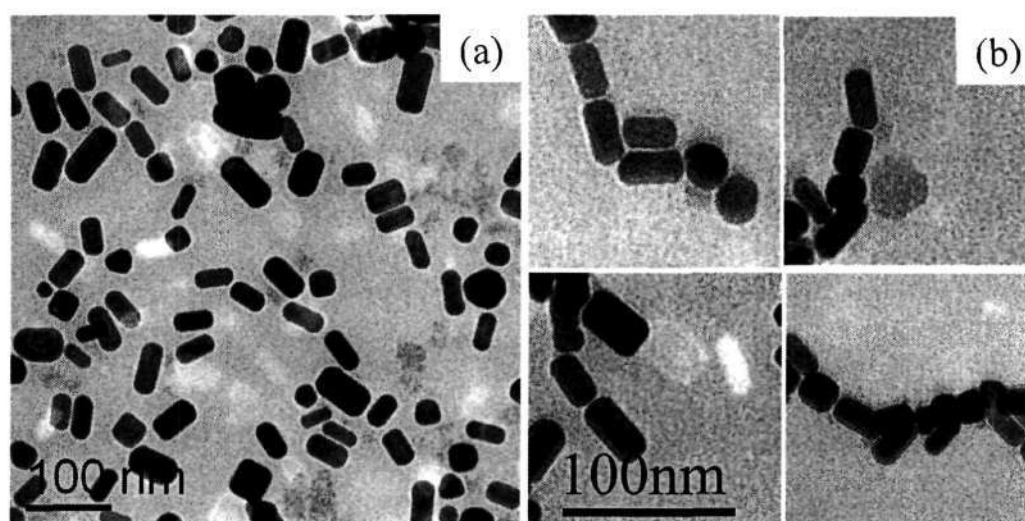
Figure 2.9 TEM micrographs of gold nanorods (a) before and (b) after the titration with MPA (scale bar – 100 nm).

Using an approach similar to that illustrated for cysteine, we have calculated the

average number of MPA molecules attached to each Au nanorod. The heat released in the

first step (Figure 2.8) is -3650 kcal/mole of Au nanorods. The number of MPA molecules

binding to each gold nanorod is therefore around 730. The heat released in the second

step is -3015 kcal per mole of gold nanorods. As intermolecular hydrogen bonding

between MPA molecules releases approximately -15 kcal/mole, the number of hydrogen

bonded units or the number of gold nanorods in the necklace cannot be greater than 200.

2.3.2 Growth of gold nanocrystals

In order to understand the thermodynamics of the growth of gold nanocrystals, we

have measured the change in heat associated with the growth of gold nanocrystals

prepared with starting $HAuCl_4$ concentrations of 0.012 and 0.018 mmol by carrying out

ITC measurements.

Figure 2.10 shows the data obtained from the ITC experiments. The red squares and green triangles correspond to data obtained for low and high concentrations of $HAuCl_4$ respectively. The data shows exothermic peaks as the heat change associated with growth is exothermic as expected.
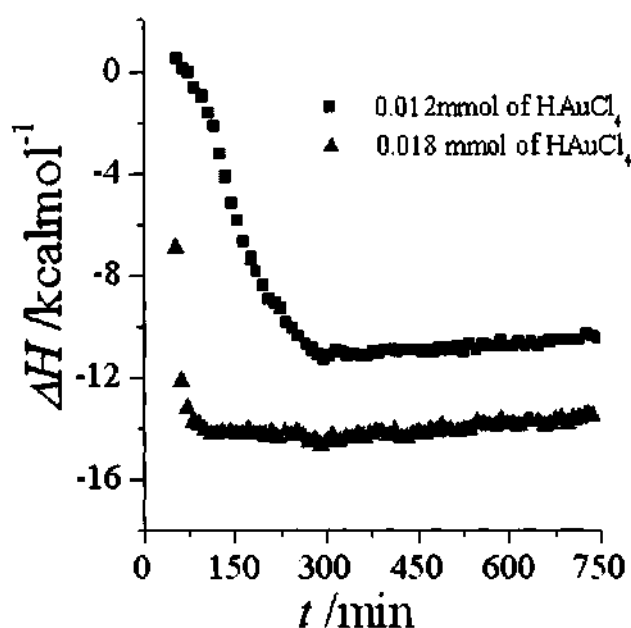
Figure 2.10 Time evolution of the heat change associated with the growth of gold nanocrystals prepared with different concentrations of $HAuCl_4$ obtained from ITC: 0.012 mmol of $HAuCl_4$ (squares) and 0.012 mmol of $HAuCl_4$ (triangles).

The exothermicity increased with progressive injection and saturated after 300min when

the concentration of the $HAuCl_4$ was 0.012 mmol as shown in Figure 2.10. In the case of

gold nanocrystals prepared with 0.018 mmol of HAuCl$_4$, the heat change saturates around

$t \approx 135$ min; compared to 300 min in the case of gold nanocrystals prepared with 0.012

mmol of HAuCl$_4$. The heat change associated with the growth of gold nanocrystals

prepared from the higher concentration of HAuCl$_4$ is larger than that found with the

lower concentration as it is evident from the figure.

We compared results obtained in ITC with the diameter changes at the same

concentration and time ranges of growth which was calculated using small angle X-ray

scattering (SAXS) and transmission electron microscopy (TEM). The diameter changes

with time for the growth for HAuCl$_4$ concentrations of 0.012 and 0.018 mmol is shown in

figure 2.11.
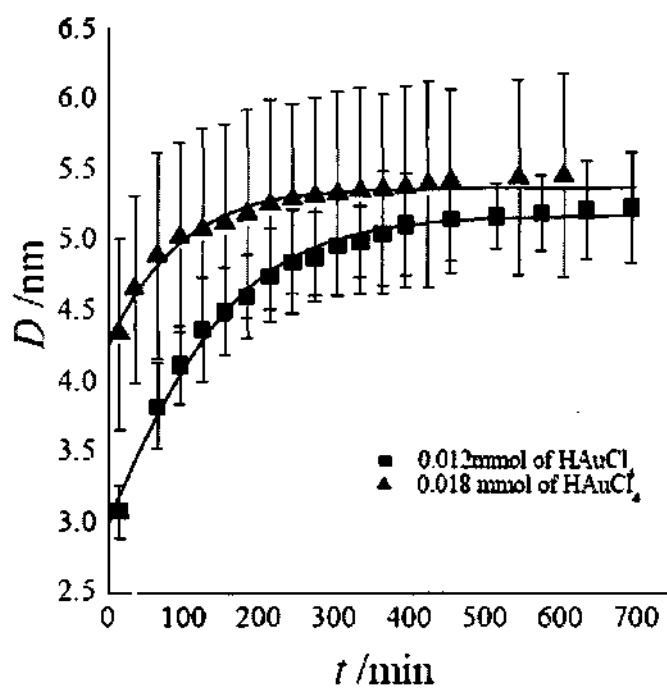
Figure 2.11 Time evolution of the average diameter (D) of the gold

nanocrystals obtained from SAXS for different concentrations of HAuCl$_4$.

The curves in Figure 2.10 show a variation opposite to that of the diameter in Figure 2.11. In both the figures the saturation time for the growth was comparable for respective concentrations. These results indicate a close relation between the variation of heat change and of the nanocrystal diameter. In Figure 2.12, we have plotted heat change associated with the growth against nanocrystal diameter by making use of the data in Figure 2.10 and Figure 2.11. The heat change varies linearly with the diameter and saturates at large diameters as shown in the figure. From the linear regime (correlation coefficients, R of 0.98 and 0.99 for 0.012 and 0.018 mmol concentrations of $HAuCl_4$ respectively), we obtain the value of heat change per nm of growth of nanocrystal. The value obtained from the slope of the linear fits are 11 and 10 kcalmol^{-1} per nm for the growth of gold nanocrystals for the starting $HAuCl_4$ concentrations of 0.012 and 0.018 mmol respectively.
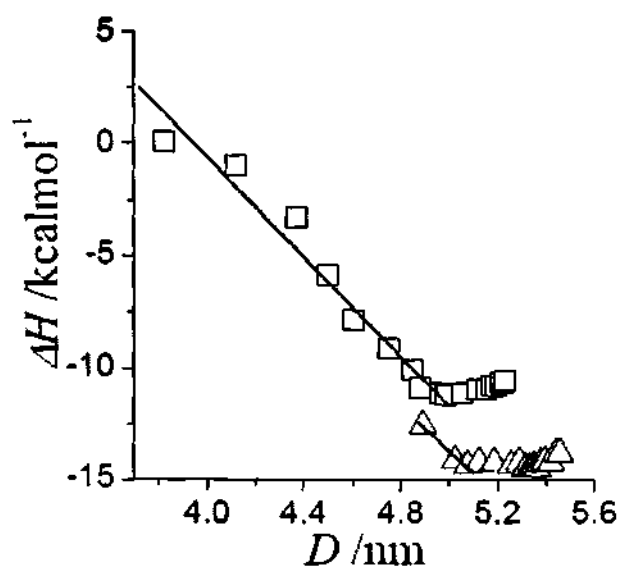
Figure 2.12 Plots of heat change associated with the growth against the diameter of the gold nanocrystal obtained from SAXS. Solid lines are the linear fit to the experimental data over the growth range.

2.3.3 Disintegration of gold films by alkanethiols

Figure 2.13 shows typical data obtained from the isothermal titration calorimetric experiments with two alkanethiols. The integrated plot of the ITC data is given after accounting for the dilution effects of alkanethiols. The additions of small amounts of alkanethiol give rise to an exothermic reaction (initial points in the curve). With increase in the thiol concentration the exothermicity decreases and the process eventually becomes endothermic. After a few injections the process again becomes exothermic. This is seen as a peak in the heat versus concentration plot (Figure 2.13).
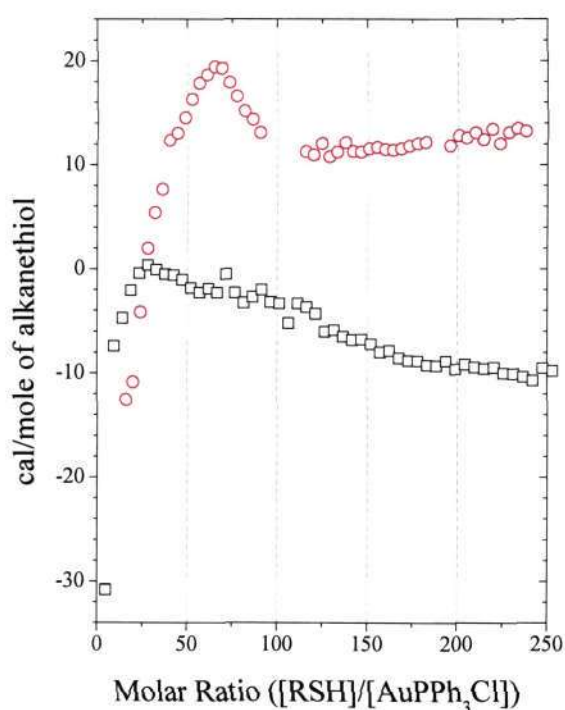
Figure 2.13 Heat content change per mole of the alkanethiols obtained by isothermal titration calorimetric (ITC) experiments versus the molar ratio of alkanethiol (a) C4 thiol, (b) C12 thiol to Au(PPh3)Cl.

Comparison of the disintegration process by two alkanethiols of different chain length (C_4, C_{12}) shows that the peak appears at different concentrations for different alkanethiols. For longer alkanethiols the peak appeared at lower concentration. The position of the peak relates to the effectiveness of the thiol in disintegrating the film. We have plotted the concentration at which the peak appears against the number of carbon atoms in the alkane chain, n in Figure 2.14. We see a near linear relationship with the peak appearing at low concentration with the increase in chain length.
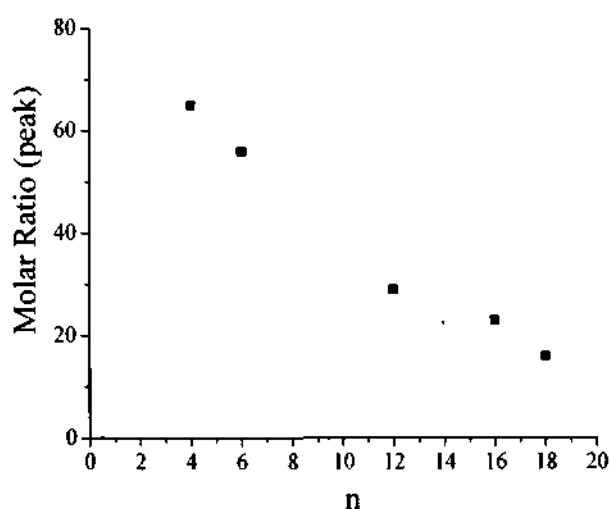
Figure 2.14 Dependence of the molar ratio of the alkanethiol to Au(PPh3)Cl at which the peak appears due to maximum endothermicity on the number of carbon atoms in the alkanethiol, *n*.

The mechanism of the disintegration of the film can be explained as follows with the help of Figure 2.15. When alkanethiols were added initially to the nanocrystalline film, the thiol group attaches to the gold nanocrystals forming Au-S bond. This step (stage 1 in Figure 2.15) corresponds to the exothermic process seen in figure 2.13. As

more alkanethiols were added to the film the number of available sites for binding on the gold nanoparticles of the film decreases which decreases the exothermicity with progressive injections. Also as the alkanethiols attaches to the nanoparticles in the film the spacing between the particles increases and the film starts to disintegrate. The endothermic process corresponds to disordering or disintegration of the film (stage 2). The more is the length of the alkanechain, the more efficient will be the disintegration process since the spacing between nanoparticles is directly proportional to the alkanethiol length. The stage 2 is more complex. After the disordering or disintegration of the film isolated nanoparticles get created which are then capped by the thiol molecules present in the solution. Hence the last step is again exothermic as indeed seen in Figure 2.13.
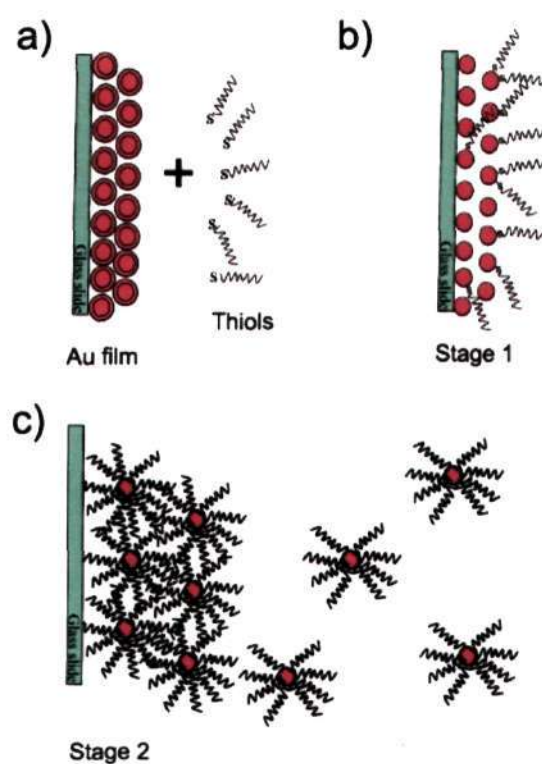
Figure 2.15 A Schematic showing the process of thiol adsorption and increasing disorder in the nanocrystalline film.

2.4 Conclusions

Isothermal titration calorimeter has been a wonderful tool to measure various interactions of nanomaterials. The process of assembly and growth of nanomaterials and disintegration of nanocrystalline film were carried out in ITC and heat changes for these processes were monitored. In the assembly process, ITC experiments were able to distinguish different kind of binding interactions. Isothermal titration calorimetric measurements on the interaction of the thiolcarboxylic acid, MPA, establishes the occurrence of two steps in the assembling process associated with the binding of gold nanorods to the sulfur atom of linker molecules and the formation of the necklace structure. The shifts of the longitudinal plasmon absorption band of the gold nanorods in the electron absorption spectrum as well as transmission electron microscope images carried out at different states of ITC measurements provide direct evidence for the occurrence of the assembly of gold nanorods at the stage expected from ITC measurements. ITC measurements on the binding of cysteine with gold nanorods show only a single step due to the binding of the molecules, since the process of assembly occurs by electrostatic interaction. Thus, measurements in the cysteine-Au nanorod systems indirectly support the mechanism for the second step found in the MPA-Au nanorod system. The growth process carried out in ITC showed consistent result with that measured using other techniques such as transmission electron microscopy (TEM), small angle X-ray scattering (SAXS). ITC measurements show the growth process of gold nanocrystals to be exothermic. The calorimetric data together with information about diameter variation helped us to calculate the heat change per nanometer (~10 kcalmol^{-1} per 1nm growth in diameter in the 3-5 nm range) for the growth of nanocrystals. The heat

change associated with the disintegration of gold nanocrystalline film formed at the liquid-liquid interface by different alkanethiols was monitored using ITC. The study gave insight to the mechanism of the disintegration and the effectiveness of the different alkanethiols in the process.

References

1. I. Jelesarov, H. R. Bosshard, J. Mol. Recognit,. **1999**, *12*, 3.

2. J. E. Ladbury, B. Z. Chowdhrv, J. Chem. Bio., **1996**, *3*, 791.

3. A. Ababou, J. E. Ladbury, J. Mol. Recognit,. **2006**, *19*, 79.

4. A. A. Saboury, J. Iran. Chem. Soc. **2006**, *3*, 1.

5. S. D. Spencer, R. B. Raffa, Pharm. Res, **2004**, *21*, 1642.

6. J. E. Ladbury, Thermochim. Acta, **2001**, *380*, 209.

7. K. Beyer, D. Leine, A. Blume, Colloids and Surfaces B: Biointerfaces , **2006**, *49*, 31.

8. O. Okhrimenko, I. Jelesarov, J. Mol. Recognit., **2008**; *21*, 1.

9. M. J. Cliff, A. Gutierrez, J. E. Ladbury, J. Mol. Recognit., **2004**, *17*, 513.

10. A. Gourishankar, S. Shukla, K. N. Ganesh, M. Sastry J. Am. Chem. Soc., **2004**, *126*, 13186.

11. A. Das , A. K. Sood, P. K. Maiti, M. Das, R. Varadarajan, C.N.R. Rao, Chem. Phys. Lett, **2008**, *453*, 266.

12. C. N. R. Rao, A. Muller, A. K. Cheetham (Eds.), Recent Advances in the Chemistry of Nanomaterials, Wiley–VCH Verlag GmbH &Co., **2004**.

13. C. N. R. Rao, G. U. Kulkarni, P. J. Thomas, P. P. Edwards, Chem. Soc. Rev., **2000**, *29*, 27.

14. E. Dujardin, L. -B. Hsin, C. R. C. Wang, S. Mann, Chem. Commun,. **2001**, 1264.

15. B. Nikoobakth, Z. L. Wang, M. A. El-Sayed, J. Phys. Chem. B, **2000**, *104*, 8635.

16. K. G. Thomas, S. Barazzouk, B. I. Ipe, S. T. S. Joseph, P. V. Kamat, J. Phys. Chem. B, **2004**, *108*, 13066.

17. S. Zhang, X. Kou, Z. Yang, Q. Shi, G. D. Stucky, L. Sun, J. Wang, C. Yan, Chem. Commun., **2007**, 1816.

18. K. K. Caswell, J. N. Wilson, U. H. F. Bunz, C. J. Murphy, J. Am. Chem. Soc., **2003**, *125*, 13914.

19. S. T. S. Joseph, B. I. Ipe, P. Pramod, K. G. Thomas, J. Phys. Chem. B, **2006**, *110*, 150.

20. R. Voggu, P. Suguna, S. Chandrasekaran, C. N. R. Rao, Chem. Phys. Lett, **2007**, *443*, 118.

21. C. N. R. Rao, G. U. Kulkarni, P. J. Thomas, V. V. Agrawal, P. Saravanan, J. Phys. Chem. B, **2003**, *107*, 7391.

22. S. Link, M. B. Mohamed, M. A. El-Sayed, J. Phys. Chem. B, **1999**, *103*, 3073.

23. C. N. R. Rao, A. Muller, A. K. Cheetham (Eds.), Nanomaterials Chemistry: Recent Developments and New Directions, Wiley–VCH Verlag GmbH&Co., **2007**.

24. G. Cao, Nanostructures & Nanomaterials: Synthesis, Properties & Applications, Imperial College Press, London, **2004**.

25. X. Peng, J. Wickham, A. P. Alivisatos, J. Am. Chem. Soc., **1998**, *120*, 5343.

26. W. W. Yu, X. Peng, Angew. Chem. Int.Ed., **2002**, *41*, 2368.

27. G. Schmid (Ed.), Clusters and Colloids. From Theory to Applications, VCH, New York, **1994**.

28. G. R. Carlow, M. Zinke-Allmang, Phys. Rev Lett., **1997**, *78*, 4601.

29. J. Alkemper, V. A. Snyder, N. Akaiwa, P. W. Voorhees, Phys. Rev. Lett., **1999**, *82*, 2725.

30. C. A. Jeffrey, E. H. Conrad, R. Feng, M. Hupalo, C. Kim, P. J. Ryan, P. F. Miceli, M. C. Tringides, Phys. Rev.Lett., **2006**, *96*, 106105.

31. S. Takakusagu, K. Fukui, R. Tero, F. Nariyuki, Y. Iwasawa, Phys. Rev. Lett., **2003**, *91*, 066102.

32. A. F. Craievich, G. Kellermann, L. C. Barbosa, O. L. Alves, Phys. Rev. Lett., **2002**, *89*, 235503.

33. R. D. Averitt, D. Sarkar, N. J. Halas, Phys. Rev. Lett., **1997**, *78*, 4217.

34. V. Arcoleo, G. Cavallaro, G. L. Manna, V. T. Liveri, Thermochim. Acta, **1995**, *254*, 111.

35. F. Aliotta, V. Arcoleo, S. Buccoleri, G. L. Manna, V. T Liveri, Thermochim. Acta, **1995**, *265*, 15.

36. W. Z. Lin, Adv. Mater., **1998**, *10*, 13.

37. C. N. R. Rao, P. J. Thomas, G. U. Kulkarni, Nanocrystals: Synthesis, Properties and Applications; Springer-Verlag: Berlin, **2007**.

38. A. H. Rechberger, A. Leitner, J. R. Krenn, B. Lamprecht, L. Aussenegg, Opt. Commun., **2003**, *220*, 137.

39. U. Kreibig, M. Vollmer, Optical Properties of Metal Clusters; Springer-Verlag: Berlin, **1995**.

40. J. B. Pelka, M. Brust, P. Gierlowski, W. Paszkowicz, N. Schell, Appl. Phys. Lett., **2006**, *89*, 063110.

41. R. H. Terrill, T. A. Postlethwaite, C.-h. Chen, C.-D. Poon, A. Terzis, A. Chen, J. E. Hutchison, M. R. Clark, G. J. Wignall, J. Am. Chem. Soc., **1995**, *117*, 12537.

42. W. P. Wuelfing, S. J. Green, J. J. Pietron, D. E. Cliffel, R. W. Murray, J. Am. Chem. Soc., **2000**, *122*, 11465.

43. M. P. Pileni, Y. Lalatonne, D. Ingert, I. Lisiecki, A. Courty, Faraday Discuss., **2004**, *125*, 251.

44. A. J. Haes, S. Zou, G. C. Schatz, R. P. VanDuyne, J. Phys. Chem. B, **2004**, *108*, 109.

45. Y. Joseph, I. Besnard, M. Rosenberger, B. Guse, H. G. Nothofer, J. M. Wessels, U. Wild, A. Knop-Gericke, D. Su, R. Schlogl, A. Yasuda, T. Vossmeyer, J. Phys. Chem. B, **2003**, *107*, 7406.

46. N. Krasteva, I. Besnard, B. Guse, R. E. Bauer, K. Mullen, A. Yasuda, T. Vossmeyer, Nano Lett., **2002**, *2*, 551.

47. Y. Lu, G. L. Liu, L. P. Lee, Nano Lett., **2005**, *5*, 5.

48. A. Yu, Z. Liang, J. Cho, F. Caruso, Nano Lett., **2003**, *3*, 1203.

49. E. Roduner, Chem. Soc. Rev., **2006**, *35*, 583.

50. C. P. Collier, T. Vossmeyer, J. R. Heath, Annu. ReV. Phys. Chem., **1998**, *49*, 371.

51. J. R. Heath, C. M. Knobler, D. V. Leff, J. Phys. Chem. B, **1997**, *101*, 189.

52. B. Kim, S. L. Tripp, A. Wei, J. Am. Chem. Soc., **2001**, *123*, 7955.

53. N. Chandrasekharan, P. V. Kamat, Nano Lett., **2001**, *1*, 67.

54. C. L. Haynes, A. D. McFarland, L. Zhao, R. P. Van Duyne, G. C. Schatz, L. Gunnarsson, J. Prikulis, B. Kasemo, M. Kall, J. Phys. Chem. B, **2003**, *107*, 7337.

55. C. N. R. Rao, G. U. Kulkarni, V. V. Agrawal, U. K. Gautam, M. Ghosh, U. Tumkurkar, J. Colloid Interface Sci., **2005**, *289*, 305.

56. V. V. Agrawal, G. U. Kulkarni, C. N. R. Rao, J. Phys. Chem. B, **2005**, *109*, 7300.

57. F. Kim, J. H. Song, P. Yang, J. Am. Chem. Soc., **2002**, *124*, 14316.

58. C. J. Orendorff, C. J. Murphy, J. Phys. Chem. B, **2006**, *110* , 3990.

59. D. G. Duff, A. Baiker, P. P. Edwards, J. Chem. Soc., Chem. Commun., **1993**, **96.**

60. H. Joshi, P. S. Shirude, V. Bansal, K. N. Ganesh, M. Sastry, J. Phys. Chem. B, *2004, 108,* 11535.

61. A. Ulman, Chem. Rev., **1996**, *96*, 1533.

Chapter 3

Investigations of the Growth Kinetics of Capped CdSe and CdS Nanocrystals by a Combined Use of Small Angle X-ray Scattering and Other Techniques

SUMMARY

The growth of capped CdSe and CdS nanocrystals formed by the reaction of selenium or sulphur with cadmium stearate in toluene solution in the presence of dodecanthiol or trioctylphosphine oxide and tetralin has been investigated by a variety of techniques such as small angle X-ray scattering (SAXS), transmission electron microscopy(TEM), and UV-visible and photoluminescence spectroscopy to obtain reliable data. By employing all these techniques we have obtained the time evolution of the average diameter $D(t)$ data and fitted then to various growth models. Although certain qualitative observations suggest growth of the nanocrystals to be controlled by diffusion-limited Ostwald ripening, we have found it is necessary to include the surface reaction term in the growth equation. Thus, growth of CdSe and CdS nanocrystals having contributions from both diffusion and surface reaction, with a D^3+D^2 type behavior, independent of the capping agent.

Introduction

The mechanism of growth of nanocrystals has attracted the attention recently in view of its importance both academically and technologically [1, 2]. A popular mechanism employed to explain the growth kinetics of nanocrystals is the diffusion-limited Ostwald ripening process following the Lifshitz-Slyozov-Wagner (LSW) theory [3, 4]. Thus, Alivisatos and coworkers [5] examined the growth of CdSe and InAs nanocrystals by employing UV-visible absorption spectroscopy to determine the size of nanocrystals and the band widths in the photoluminescence spectra to determine their size distribution and observed a focusing and defocusing effect of the size distribution similar to that expected in Ostwald ripening. Qu et al. [6] noted a asymmetric diameter distribution similar to that expected for diffusion-limited Ostwald ripening at last stage of the growth mechanism in the case of CdSe nanocrystals. Peng and Peng [7, 8] examined the growth kinetics of CdSe nanorods by UV- vis spectroscopy and transmission electron microscopy (TEM) and found the diffusion-controlled model to be valid when the monomer concentration was sufficiently high. Searson and coworkers [9-11] find the growth of ZnO and TiO$_2$ nanocrystals to follow Ostwald ripening as the dominant mechanism. Our own study of growth kinetics of uncapped ZnO nanorods [12] has shown a diffusion-controlled growth. Based on an *in-situ* TEM investigation, El-Sayed and coworkers [13] report a diffusion-controlled growth of small gold nanoclusters.

There are several reports in the literature where the growth kinetics of nanocrystals is observed to deviate from the simple diffusion-limited Ostwald ripening model. Thus, Seshadri et al. [14] propose the growth of gold nanocrystals to be essentially stochastic wherein the nucleation and growth steps are well separated. A

recent study of the nucleation and growth of gold nanocrystals by SAXS and UV-visible spectroscopy over very short time scale suggests a surface reaction-limited growth of nanocrystals in the presence of an alkanoic acid [15]. The slow growth kinetics of gold nanocrystals has been recently reported to follow a sigmoidal growth law rather than ostwald ripening [16]. Sarma and coworkers [17] report the growth kinetics of CdS and ZnS nanocrystals by small angle X-ray scattering (SAXS) not to follow the Ostwald ripening model. These workers also report the growth kinetics of the ZnO nanocrystals in the absence of any capping agent to deviate from diffusion-controlled Ostwald ripening [18, 19]. These studies as well as theoretical studies of Talapin et al. [20] suggest that the growth kinetics of nanocrystals are best explained on the basis of a combined model containing diffusion of monomers as well as the reaction at the surface. Growth kinetics of nanocrystals in the presence of capping agents is controlled by several factors, and signatures of either the diffusion or the surface reaction-controlled regimes are seen. The effect of capping agents on the growth of nanocrystals has been examined by a few workers [5-8, 21-27]. For example, the growth kinetics of ZnO nanorods in the presence of poly(vinyl pyrollidone) (PVP) is best explained on the basis of a combined growth model involving both diffusion and surface reaction [12].

3.1   Scope of the present investigation

In view of the importance of understanding of the detailed growth mechanism of II-VI semiconductor nanocrystals, we considered it valuable to investigate the growth kinetics of CdSe and CdS nanocrystals over relatively long periods by employing a variety of techniques.   Most of the studies of the growth kinetics of CdSe and CdS

nanocrystals reported in the literature are based on UV-vis and photoluminescence spectroscopies, which are indirect and are strongly affected by the change in the electronic structure of the nanomaterials. We have therefore employed SAXS along with TEM and UV-vis and photoluminescence spectroscopy for our study of the growth kinetics of CdSe and CdS nanocrystals. Employing such independent techniques is important because of the limitations of each of the techniques. SAXS provides a direct probe to determine the size and shape of nanomaterials and the sampling size is very much larger than that in TEM measurements. Additionally, SAXS is most suited for an *in-situ* study of the growth of nanocrystals. We have also obtained the size distribution of the nanocrystals by TEM at different time of growth. While TEM is the most direct probe to obtain the size, shape and size distribution of nanostructures, it is not possible to carry out *in-situ* measurements, especially when the initial nanostructures are small in size.

We have employed a solvothermal reaction between cadmium stearate [Cd(st)$_2$] and Se or S powder in the presence of dodecanthiol or trioctylphosphine oxide (TOPO) in toluene and a catalytic amount of tetralin [28, 29]. We have obtained growth kinetic data starting with different initial concentrations of Cd(st)$_2$ and report the results of this study in this article. Our study has provided good kinetic data on the growth of CdSe and CdS nanocrystals. The data, however, do not conform to diffusion-limited Ostwald ripening in both the cases. The growth mechanism in the case of both CdSe and CdS nanocrystals deviates from the diffusion-limited LSW model requiring an additional contribution from a surface process.

3.2 Experimental section

Synthesis of CdSe nanocrystals

In order to carry out the growth study, CdSe nanocrystals were prepared by the reaction of cadmium stearate and selenium powder in toluene at 250 °C under solvothermal conditions as reported in the literature [28]. The reaction was stopped at different times (1, 2, 3, 4, 5 and 10 h) and the products were analyzed by TEM and SAXS, UV-vis and photoluminescence spectroscopy. In a typical synthesis, cadmium stearate (0.2 g, 0.29 mmol) and selenium powder (0.023 g, 0.29 mmol) were added to 20 mL toluene, followed by the addition of 30.4 µL tetralin and 17.4 µL of 1-dodecanethiol . The reaction mixture was sealed in a Teflon-lined autoclave (60% filling fraction) and maintained at 250 °C in a hot air oven. The solid products obtained at different times after the reaction were precipitated with addition of 2-propanol. The precipitate was collected by centrifugation and redissolved in Toluene. To study the effect of the concentration of the reactants on the growth process, we prepared CdSe nanocrystals at lower concentration of cadmium stearate (0.05g, 0.07mmol) keeping the other reaction parameters the same. The samples were taken out after different reaction times (2, 3, 4, 5 and 10h) for investigation. To study the effect of the capping on the growth process, we prepared CdSe nanocrystals using trioctylphosphine oxide, TOPO, as capping agent (0.0038 g, 0.00 9mmol) instead of 1-dodecanethiol keeping the other reaction parameters the same. The samples were taken out after different reaction times (2, 3, 4, 5 and 10h) for investigation.

Synthesis of CdS nanocrystals

In order to carry out the growth study, CdS nanocrystals were prepared by the reaction of cadmium stearate and sulphur powder in toluene at 250 °C under solvothermal conditions as reported in the literature [29]. The reaction was stopped at different times (1, 2, 3, 4, 5 and 10 h) and the products were analyzed by TEM and SAXS, UV-vis and photoluminescence spectroscopy. In a typical synthesis, cadmium stearate (0.05 g, 0.07 mmol) was dissolved in 20 mL toluene, and sulphur powder (2.4 mg, 0.07 mmol), 30.4 μL tetralin and 17.4 μL of 1-dodecanethiol were added under stirring. The reaction mixture was sealed in a Teflon-lined autoclave (60% filling fraction) and maintained at 250 °C in a hot air oven. The solid products obtained at different times after the reaction were precipitated with addition of 2-propanol. The precipitate was collected by centrifugation and redissolved in Toluene.

SAXS characterization

The average diameter of the CdSe and CdS nanocrystals could be readily obtained by SAXS [31-33]. We performed SAXS experiment with a Bruker-AXS NanoSTAR instrument modified and optimized for solution scattering. The instrument is equipped with a X-ray tube (Cu Kα radiation, operated at 45 kV/35 mA), cross-coupled Göbel mirrors, three-pinhole collimation, evacuated beam path, and a 2D gas-detector (HI-STAR) [33]. The accessible scattering range of the instrument can be varied by selecting different distances between the sample and the detector of 42.2 cm and 66.2 cm. The modulus of the scattering vector is $q = 4\pi Sin\theta/\lambda$, where θ is scattering angle and λ is X-ray wave length. We recorded the SAXS data in the q = 0.007 to 0.21 Å^{-1} range, i.e, 2θ =

0.1 to 3°. Solutions of the CdSe and CdS nanocrystals in toluene (approximate 0.1 w/v % concentration) obtained after lapse of different reaction times were used for SAXS measurements. The solutions of nanocrystals were taken in quartz capillaries (diameter of about 2 mm) for the measurements with an exposure time of 20 min in order to obtain good signal-to-noise ratios. A capillary filled with only toluene was used for background correction. The concentration of the nanocrystals was sufficiently low to neglect interparticle interference effects. The experimental SAXS data were fitted by Bruker-AXS DIFFRAC^{plus} NANOFIT software by using solid sphere model. The form factor of the spheres used in this software is that due to Rayleigh [34]. The assumption of the spherical model was verified by carrying out TEM investigations at several points of the growth process.

TEM characterization

The solid products obtained after different reaction periods were dissolved in toluene and were taken on holey carbon-coated Cu grids for TEM investigations with a JEOL (JEM3010) microscope operating with an accelerating voltage of 300 kV. The diameter distributions were obtained from the magnified micrograph by using DigitalMicrograph 3.4 software.

UV-visible and photoluminescence

The UV-visible spectroscopy measurements were performed using a Perkin-Elmer Lambda 900 UV/VIS/NIR spectrometer. The nanocrystals were dissolved in toluene and the solution was used to carry out the UV-vis measurements. Photoluminescence spectra of these solutions were recorded with a Perkin-Elmer model

LS55 luminescence spectrometer. The average diameter of the nanocrystals was calculated from the absorption peak position using the sizing curves given in the literature [35]. The Sizing curves provided the diameter of CdSe and CdS nanocrystals which was calculated by TEM and XRD versus its first absorption peak position.

3.3   Results and Discussion

SAXS measurements on the growth of dodecanethiol-capped CdSe nanocrystals were carried out at different initial concentrations of $Cd(st)_2$. In Figures 3.1a and 3.1b, we show typical logarithmic scale plots of intensity vs. scattering vector for different times of growth in the case of nanocrystals prepared with (0.05g, 0.07mmol) and (0.2 g, 0.29 mmol) of $Cd(st)_2$ respectively.
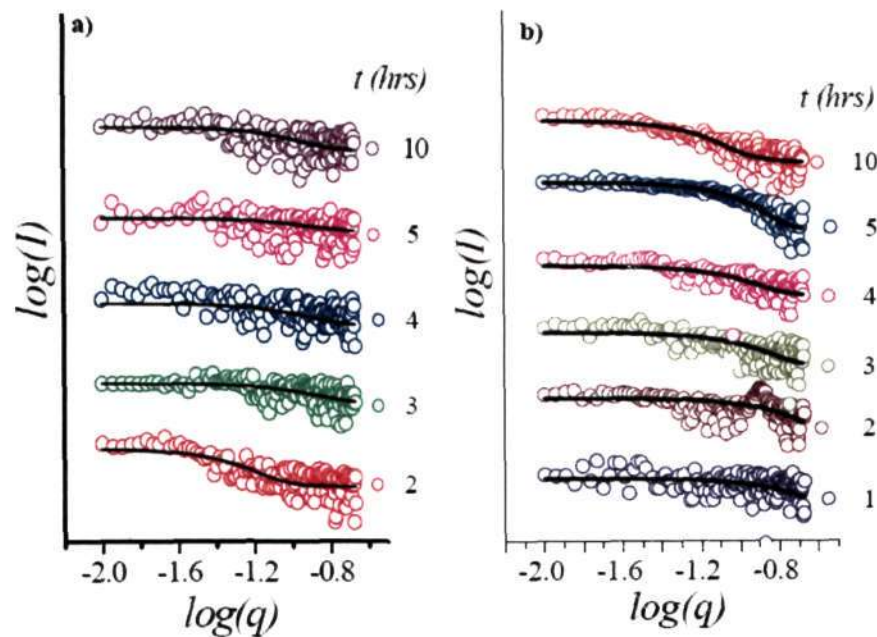
Figure 3.1 SAXS data for the growth of CdSe nanocrystals prepared from a) 0.05g (0.07 mmol), and b) 0.2g (0.29 mmol) of cadmium stearate after different times of the reaction. Solid lines are the spherical model fits to the experimental data.

The changes observed in the SAXS patterns clearly indicate that the nanocrystals grow as a function of time at both the concentrations of $Cd(st)_2$. In order to estimate the average diameter and diameter distribution of CdSe nanocrystals, we have fitted the experimental SAXS data to the spherical model mentioned in experimental section. The scattering contrast for X-rays is given by the electron density difference between the particle and the solvent. Since CdSe has higher contrast than the solvent, only the CdSe particles need to be considered for analysis.

In the case of a diluted assembly of spherical particles, neglecting particle interaction, the scattering intensity is given by,

$$I(q) \propto \int f(R)V(R)^2 P(q,R)dR \tag{1}$$

where $V(R)$ and $P(q, R)$ are the volume and form factor respectively of a sphere of radius R. The form factor of the sphere is given by,

$$P(q,R) = \left[\frac{3\{\sin(qR) - qR\cos(qR)\}}{(qR)^3} \right]^2 \tag{2}$$

In Eq. (2), q is the scattering vector ($q = 4\pi Sin\theta/\lambda$, where θ is scattering angle and λ is X-ray wave length), and R the radius of the sphere. To obtain the particle size distribution, we used the Gaussian distribution, $f(R)$,

$$f(R) = \frac{1}{\sigma\sqrt{2\pi}} e^{-\left[(R-R_0)^2/2\sigma^2\right]} \tag{3}$$

Least square refinement yields two parameters, R and σ where the latter is the standard deviation. The solid curves in the Figure 3.1 are the sphere model fits of the experimental

SAXS data. The fits with the experimental patterns are quite good, yielding the average diameter as well as the diameter distributions for different growth times.

We have estimated the diameter, D, of the CdSe nanocrystals after different periods of growth from the SAXS data, and show the time evolution of the diameter distribution in Figure 3.2a in the case of nanocrystals prepared with (0.2 g, 0.29 mmol) of $Cd(st)_2$. Figure 3.2b represents the corresponding time evolution of the standard deviation of the diameter distribution, σ_D (i.e. half-width of the diameter distribution). The width of the diameter distribution increases up to certain time, undergoes a sudden drop and finally reaches a maximum value. We have observed a similar fluctuation in the diameter distribution in the case of CdSe nanocrystals prepared from a lower concentration of $Cd(st)_2$. Such focusing and defocusing of the diameter and length distributions has been noticed earlier in the case of CdSe nanoparticles [5] and of ZnO nanorods [12]. When the monomer concentration gets depleted due to the faster growth of the nanocrystals, the smaller nanocrystals start to shrink while the bigger ones keep growing. The size distribution, therefore, becomes broader (e.g., t = 3 hrs). Dissolution of the small nanocrystals again enriches the monomer concentration in the solution, with the growth of the bigger nanocrystals continuing through the diffusion of the monomer from solution to the nanocrystals surface, giving rise to focusing of the diameter distribution (e.g., t = 4 to 5 hrs). Focusing and defocusing of the diameter distribution is thus dependent on the variation of the monomer concentration in the solution, indicates that the growth of CdSe nanocrystals occurs at least partly by the diffusion of monomer from solution to surface of the nanocrystals.
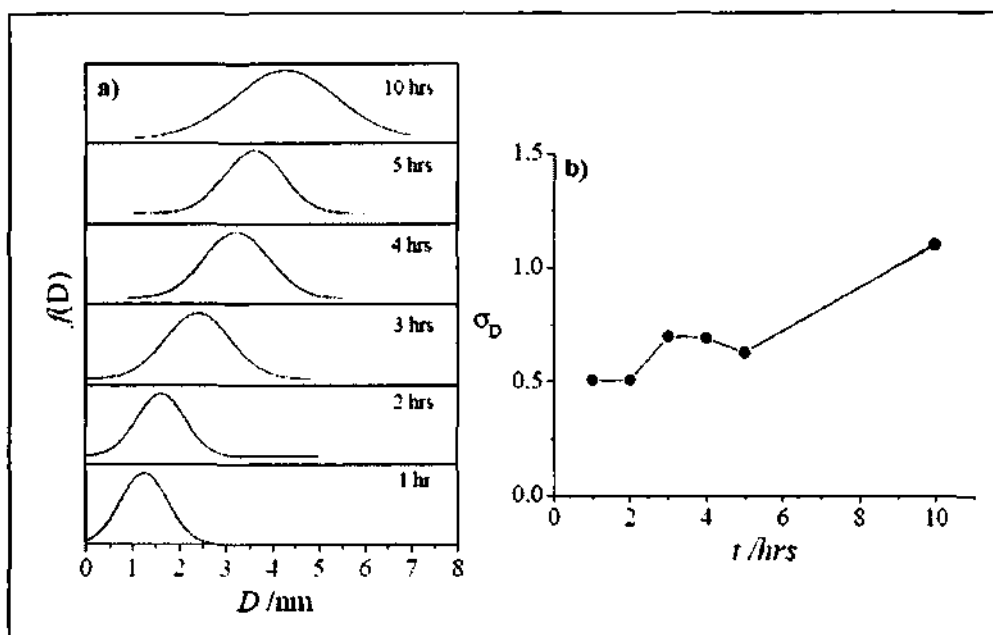
Figure 3.2 a) Time evolution of diameter distribution of the CdSe nanocrystals prepared from 0.2g (0.29 mmol) of cadmium stearate and b) the corresponding time evolution of the standard deviation, σ_D, of diameter distribution. The distributions are obtained from the spherical model fits to the experimental SAXS data, recorded after different reaction times (1-10 hrs).

We have carried out TEM measurements at a few points during the growth of the CdSe nanocrystals. In Figure 3.3, we show typical TEM images of CdSe nanocrystals prepared with (0.2 g, 0.29 mmol) of $Cd(st)_2$ after different periods of growth to illustrate how the size of the CdSe nanocrystals increases with increasing growth time. We have estimated the average diameter and the diameter distribution of CdSe nanocrystals at different stages of the growth from the TEM images. Although the TEM data are not statistically as satisfactory as SAXS, the diameter distributions obtained from TEM and SAXS after 3, 4, 5 and 10 h of growth show good agreement.
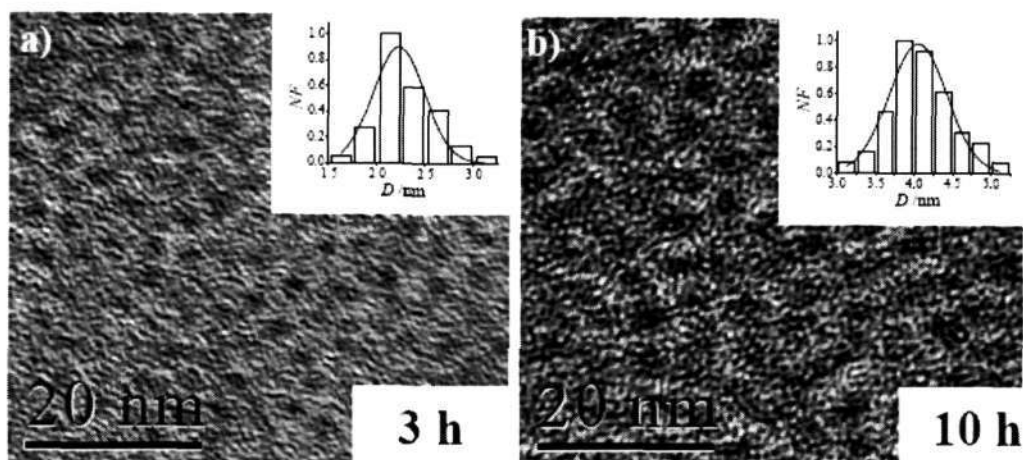
Figure 3.3 TEM images of CdSe nanocrystals prepared from 0.2g (0.29 mmol) of cadmium stearate obtained after a) 3 and b) 10hrs of growth. Insets show the diameter distributions obtained from TEM. NF: normalized frequency.

We have also carried out the UV-vis and PL spectroscopy measurements to obtain additional information on the growth kinetics of CdSe nanocrystals. Figures 3.4a and b respectively represent the time evolution of UV-vis and PL spectra of the CdSe nanocrystals prepared from (0.2 g, 0.29 mmol) of Cd(st)$_2$. The UV-vis spectra show three clearly resolved bands around 410, 458 and 505 nm after 3 h of the reaction, consistent with the literature [5, 28, 30]. With increasing reaction time, the absorption bands of CdSe nanocrystals are red-shifted from 400 to 600 nm as the particle size increases. We have calculated the average diameters of the CdSe nanocrystals after different times of the reaction from the UV-vis spectra following the method described in the experimental section.
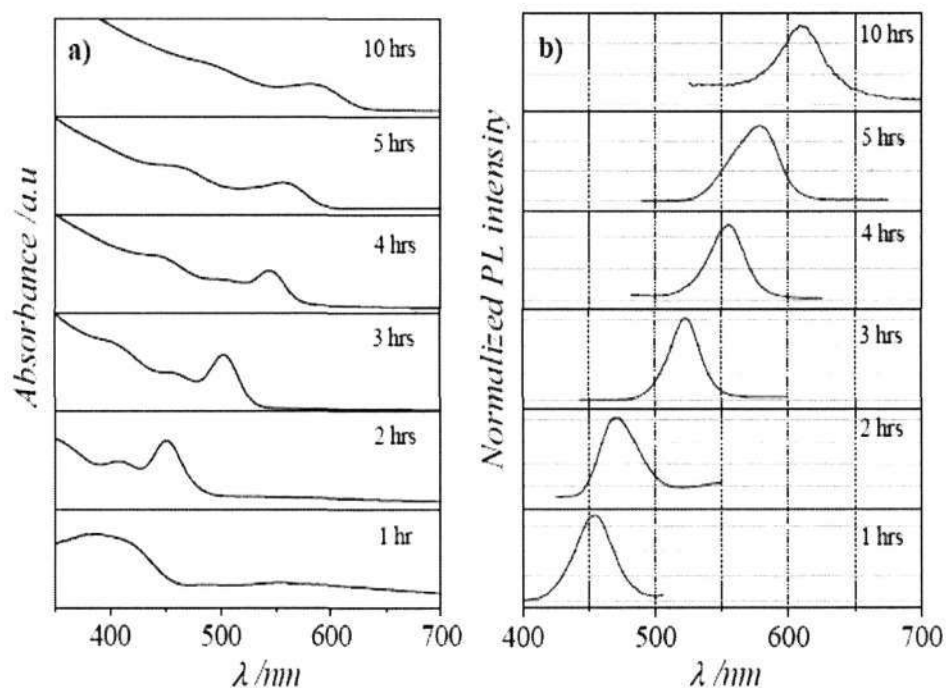
Figure 3.4 a) UV-vis spectra and b) photoluminescence spectra of CdSe nanocrystals prepared from 0.2g (0.29 mmol) of cadmium stearate obtained after different time of growth (1-10hrs).

The PL spectra of CdSe nanocrystals in Figure 3.4b show clearly resolved band edge luminescence (e.g., 518 nm band after 3 h of reaction), consistent with the literature [5, 6, 28, 30]. The PL band of CdSe nanocrystals is red-shifted from 455 to 615 nm with increasing reaction time. The width of the PL spectra also provides the information of the particle size distribution [6]. The width of the PL band changes with the increase in reaction time similar to that observed in the case of the width of diameter distribution (Figure 3.2). The diameter distributions derived from PL bands are similar to those from SAXS, the focusing and defocusing of the PL band width with reaction time [6]. Surprisingly the PL bands become symmetric (t = 1, 3, 4 and 10 h) and asymmetric (t =

2 and 5 h) during the growth of the particle. The LSW theory of growth predicts an
asymmetric size distribution [2, 3]. Thus, the PL data reveal diffusion-limited reaction
contributes to the growth of CdSe nanocrystals.

In figure 3.5, we have shown the time evolution of the average diameter obtained
from SAXS (filled circles), TEM (open circles) and UV-vis spectroscopy (open triangles)
of the CdSe nanocrystals prepared with two different concentrations of $Cd(st)_2$
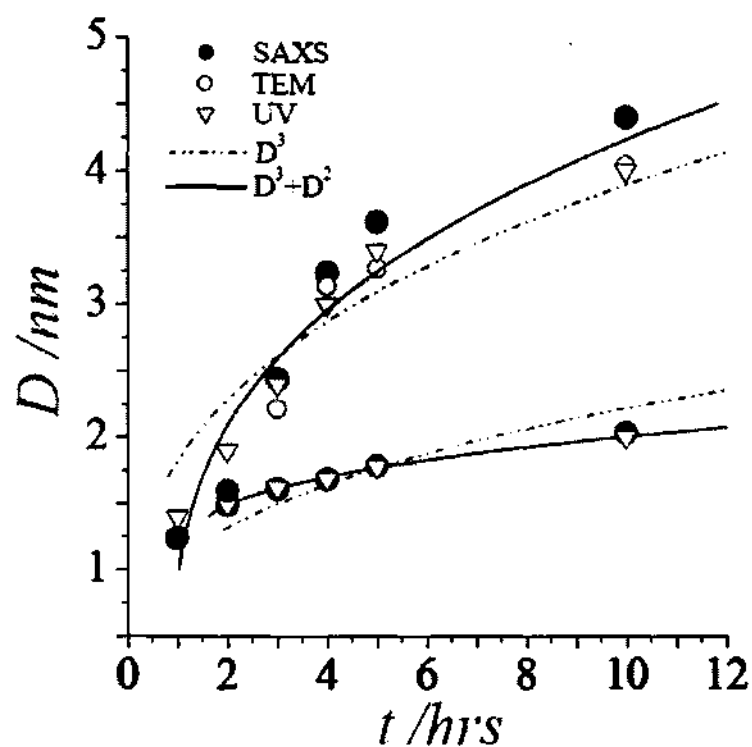
Figure 3.5 Time evolution of the average diameter (D) of the CdSe nanocrystals
obtained from SAXS for different concentrations cadmium stearate (filled
circles). TEM data are shown by open circles. Average diameter calculated from
UV-vis spectra are given by open triangles. Solid curves represent fits of the data
to the combined surface and diffusion growth model. Dotted curve is the Ostwald
ripening model fit to the experimental data.

The diameters obtained from different techniques are in close agreement. The diameter of the CdSe nanocrystals varies from 1 to 2.1 nm and from 1.3 to 4.4 nm when the starting $Cd(st)_2$ concentrations are 0.07 and 0.29 mmol respectively. With increasing concentration of $Cd(st)_2$, the diameter of CdSe nanocrystals increases, higher monomer concentrations favoring the formation of bigger CdSe nanocrystals.

Although some qualitative evidence for the diffusion-limited growth of CdSe nanocrystals is provided by the observation of the focusing and defocusing diameter distribution, a better insight is obtained from the time evolution of the average diameter of nanocrystals. If the diffusion-limited Ostwald ripening according to LSW theory [3, 4] were the sole contributor for the growth, the rate law would be given by [2]

$$D^3 - D^3{}_0 = Kt \qquad (4)$$

where D is the average diameter at time t and D_0 average initial diameter of the nanocrystals. The rate const K is given by $K = 8\gamma dV_m{}^2 C_\infty / 9RT$, where d is the diffusion constant at temperature T, V_m the molar volume, γ the surface energy, and C_∞ the equilibrium concentration at a flat surface. We have tried to fit the $D(t)$ data of the CdSe nanocrystals obtained from SAXS, TEM and UV-vis spectroscopy to the Ostwald ripening model and found that it was not possible to fit the $D(t)$ data by Eq. (4). A typical fit to the Eq. (4) of the $D(t)$ data of the CdSe nanocrystals obtained is shown in Figure 3.5 by the broken curve. The fit is not satisfactory with a coefficient of determination, R^2, of 0.33 and 0.58 for 0.07 and 0.29mmol of $Cd(st)_2$. The growth process clearly deviates from diffusion-limited Ostwald ripening. We have tried to fit the $D(t)$ data to the surface-

limited reaction model ($D^2 \propto t$)or by varying the value of the exponent (n in $D^n \propto t$,)

and found that the fit of the data was unsatisfactory to both the surface reaction model

and to a variable n model [2]. In order to fit the experimental $D(t)$ data of the CdSe

nanocrytals, we have, therefore, used a model which contains both the diffusion-limited

and surface-limited growth, [2, 12, 19]

$$BD^3 + CD^2 + const = t \qquad (5)$$

where, $B = AT/\exp(-E_a/k_B T)$, $A \propto 1/(D_0 \gamma V_m^2 C_\infty)$ and $C \propto T/(k_d \gamma V_m^2 C_\infty)$, k_d is the

rate constant of surface reaction. The goodness of fits with $R^2 = 0.99$ and 0.97 for the

lower and higher concentrations of Cd(st)$_2$ respectively over the entire range of

experimental data by the combined diffusion and surface reaction control model is shown

by thick solid curve in the Figure 3.5. The growth of the CdSe nanocrystals thus appears

to have contributions from surface reaction as well.

We have studied the effect of a capping agent on the growth kinetics of CdSe

nanocrystals. For this purpose, we have employed TOPO in place of dodecanethiol

keeping the other conditions same at the time of the reaction. We have estimated the

diameters and diameter distributions of TOPO-capped CdSe nanocrystals after different

times of the reaction by SAXS, TEM, UV-vis and photoluminescence like dodecanethiol-

capped CdSe nanocrystals. In Figure 3.6, we show the average diameter of TOPO-capped

CdSe nanocrytals obtained from SAXS, TEM and UV-vis spectroscopy after different

times of the reaction. Diameters obtained from the different techniques show close

agreement. The diameter of the CdSe nanocrystals varies from 1.1 to 2.7 nm when the

starting Cd(st)$_2$ concentration is 0.29 mmol. In the presence of TOPO, the increase in

diameter is somewhat smaller compared to the dodecanethiol-capped case. We have found Ostwald ripening model [Eq. (4)] to be unsatisfactory for the data with TOPO as capping agent as well. The surface-limited reaction model or by variation of the exponent (n in $D^n \propto t,$) does not show good agreement with experiment. We have therefore used the combined model, Eq. (5), containing both diffusion-limited and surface-limited growth. The fit is good over the entire rage of the data ($R^2 = 0.997$, solid curve in Figure 3.6). Thus, the growth of the TOPO-capped CdSe also follows the combined diffusion and surface reaction-control model.
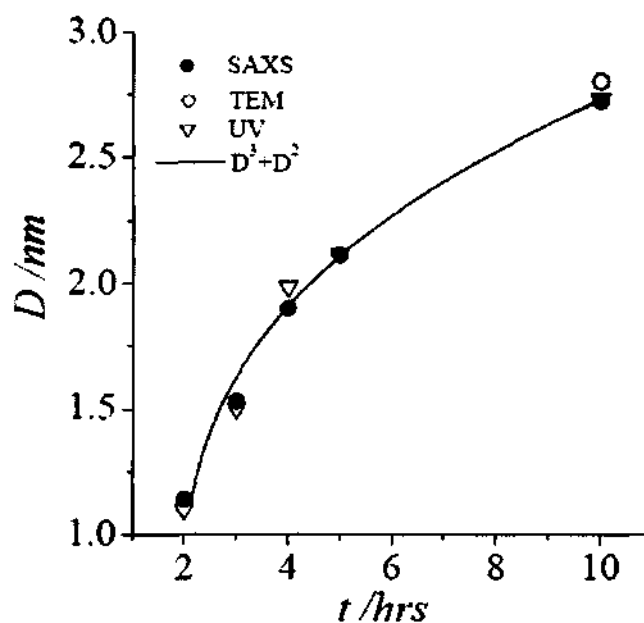
**Figure 3.6** Time evolution of the average diameter (D) of the CdSe nanocrystals obtained from SAXS using TOPO as the capping agent (filled circles). TEM data are shown by open circles. Average diameter calculated from UV-vis spectra are given by open triangles. Solid curves represent the combined surface and diffusion growth model fits to the experimental data.

We have carried out studies on the growth kinetics of the dodecanethiol-capped CdS nanocrystals by a combined use of SAXS, TEM and UV-vis/photoluminescence spectroscopy. Figure 3.7 shows typical intensity vs. scattering vector plots in the logarithmic scale for different times of growth in the case of CdS prepared with (0.05g, 0.07mmol) of $Cd(st)_2$. In order to estimate the average diameter and diameter distribution of CdS nanocrystals, we have fitted the experimental SAXS data to the spherical model. The width of the diameter distribution obtained from SAXS show the similar focusing and defocusing observed in the case of CdSe nanocrytsals.
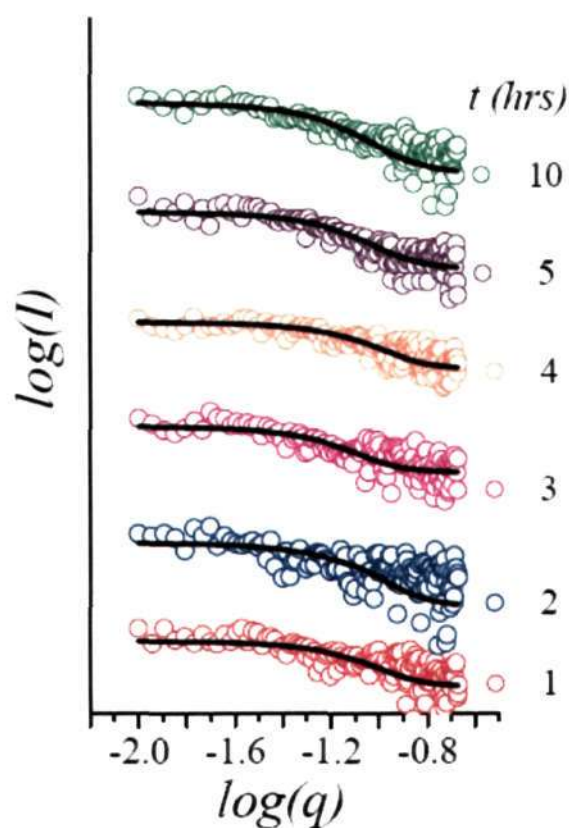
Figure 3.7 SAXS data for the growth of CdS nanocrystals prepared from a)0.05g (0.07 mmol) of cadmium stearate after different times of the reaction. Solid lines are the spherical model fits to the experimental data.

We have also carried out TEM measurements on the CdS nanocrystals at a few points during the growth and we show typical TEM images of CdS nanocrystals prepared with (0.05 g, 0.07 mmol) of Cd(st)$_2$ after different periods of growth in Figure 3.8. We have estimated the average diameter and the diameter distribution of CdS nanocrystals at different stages of the growth from the TEM images. Although the TEM data are not expected to as statistically satisfactory as SAXS, the diameter distributions obtained from TEM and SAXS after 4 and 10 h of growth are in good agreement.
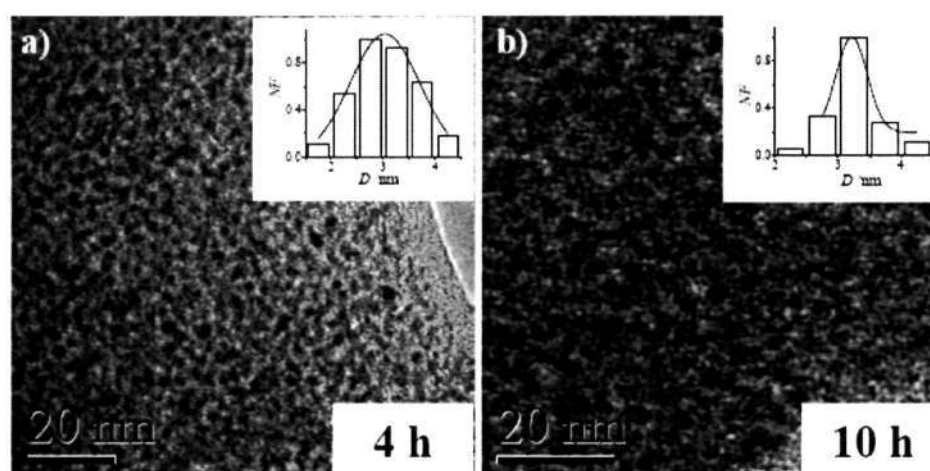
Figure 3.8 TEM images of CdS nanocrystals prepared from 0.05g (0.07 mmol) of cadmium stearate obtained after a) 4 and b) 10hrs of growth. Insets show the diameter distributions obtained from TEM. NF: normalized frequency.

Figure 3.9 represents the time evolution of UV-vis spectra of the CdS nanocrystals prepared from (0.05 g, 0.07 mmol) of Cd(st)$_2$. The UV-vis spectra show one transition (e.g., 375 nm band after 3 h of the reaction), consistent with the literature [30]. With increasing reaction time, absorption bands of CdS nanocrystals are red-shifted from 360 to 390 nm as the particle size increases. The PL spectra of CdS are not as good as

those CdSe. We have the band-edge luminescence at about 370 nm after 2 h of the reaction.
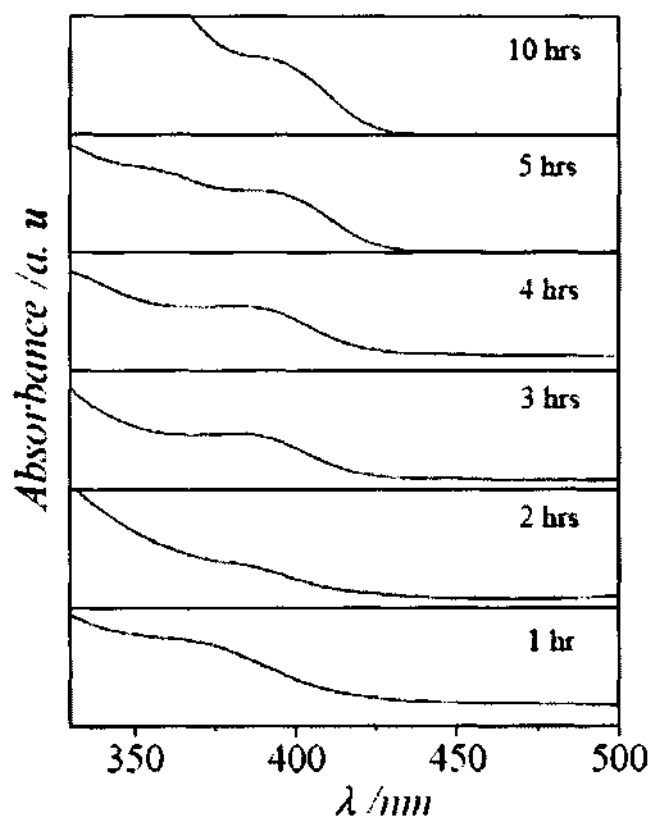
Figure 3.9 UV-vis spectra of CdS nanocrystals prepared from 0.05g (0.07 mmol) of cadmium stearate obtained after different time of growth (1-10hrs).

We have plotted the average diameter obtained from SAXS (filled circles), TEM (open circles) and UV-vis spectroscopy (open triangles) of CdS nanocrystals against time in Figure 3.10. Diameters obtained from different techniques exhibit close agreement. The diameter of the CdS nanocrystals varies from 2.3 to 3.1 nm when the starting $Cd(st)_2$ concentration is 0.07 mmol. We have tried to fitted the $D(t)$ data to the Ostwald ripening model [Eq. (4)] and found that it was not possible to do so, the R^2 value being only 0.85.

A typical fit of the $D(t)$ data to Eq. (4) of the CdS nanocrystals is shown in Figure 3.10 by the broken curve. The growth process clearly deviates from diffusion-limited Ostwald ripening. We have found good fit of the data only with the combined model, Eq. (5), containing both diffusion-limited and surface-limited growth. The fit is good over the entire rage of the data ($R^2 = 0.99$, solid curve in Figure 10). Thus, the growth of the CdS deviates sufficiently from the diffusion-limited Ostwald ripening model and follows a mechanism involving both diffusion-control and surface reaction control.
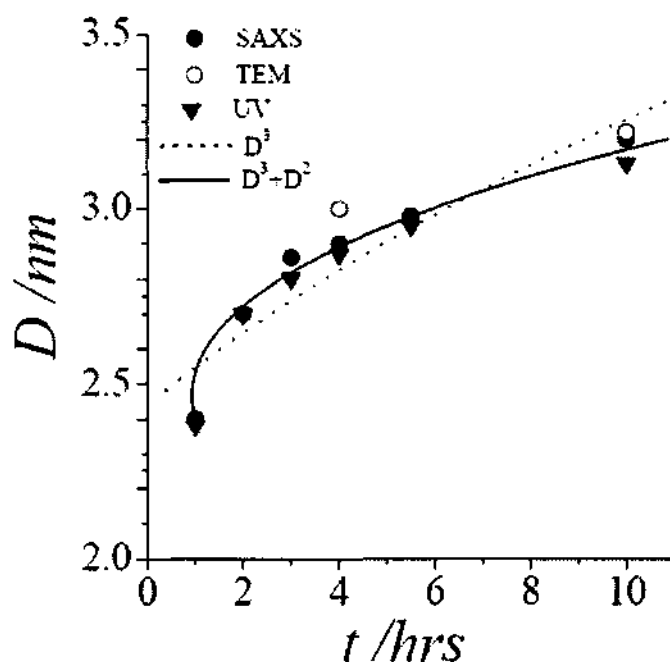
Figure 3.10 Time evolution of the average diameter (D) of the CdS nanocrystals obtained from SAXS for 0.05g (0.07 mmol) of cadmium stearate (filled circles). TEM data are shown by open circles. Average diameter calculated from UV-vis spectra are given by solid triangles. Solid curves represent the combined surface and diffusion growth model fits to the experimental data. Dotted curve is the Ostwald ripening model fit to the experimental data.

The growth of the nanocrystals mainly occurs by the diffusion of monomers from solution to the nanocrystal surface or by the reaction at the surface where units of the diffusing particles get assimilated into the growing nanocrystals. Diffusion and surface reaction are limiting cases in nanocrystal growth. The presence of capping agent in the both the cases, gives rise to a barrier to diffusion. The contribution of the surface reaction, therefore, comes into picture. The growth of capped CdSe and CdS nanocrystals clearly occurs through a combination of diffusion and surface reaction processes.

3.4   Conclusions

A systematic study of the growth of capped CdSe and CdS nanocrystals has been carried out by a combined use of SAXS, TEM, UV-vis and PL spectroscopy to obtain reliable data on the growth kinetics. The rate of growth was sufficiently slow to follow the kinetics over a long period. Thus, the data represent the kinetics of the growth immediately after the nucleation which probably occurs within a minute or so. With increasing concentration of the starting metal precursor, $Cd(st)_2$, the diameter of the CdSe nanocrystals increases. Focusing and defocusing of the diameter distribution and the asymmetric nature of the PL band of the nanocrystals reveal that the diffusion of the monomer contributes towards the growth of the nanocrystals. However, the best fits of the $D(t)$ data is found to a D^3+D^2 model, suggesting that the growth mechanism of capped CdSe and CdS nanocrystals involves both diffusion and surface reactions. The presence of a capping agent, gives rise to a barrier to diffusion, thereby rendering the contribution of the surface reaction relevant.

References

1. C. N. R. Rao, P. J. Thomas, G. U. Kulkarni, Nanocrystals: Synthesis, Properties and Applications, Springer, **2007**.

2. Eds. C. N. R. Rao, A. Muller, A. K. Cheetham: Nanomaterials Chemistry:Recent Developments and New Directions, Wiley-VCH , Weinheim. **2007**.

3. I. M. Lifshitz, V. V. Slyozov, J. Phys. Chem. Solids, **1961**, *19*, 35.

4. C. Wagner, Z. Elektrochem., **1961**, *65*, 581.

5. X. Peng, J. Wickham, A. P. Alivisatos, J. Am. Chem. Soc. **1998**, *120*, 5343.

6. L. Qu, W. W. Yu, X. Peng, Nanolett. **2004**, *4*, 465.

7. Z. A. Peng, X. Peng, J. Am. Chem. Soc. **2001**, *123*, 1389.

8. Z. A. Peng, X. Peng, J. Am. Chem. Soc. **2002**, *124*, 3343.

9. E. M. Wong, J. E. Bonevich, P. C. Searson, J. Phys. Chem. B **1998**, *102*, 7770.

10. Z. Hu, D. J. E. Ramírez, B. E. H. Cervera, G. Oskam, P. C. Searson, J. Phys. Chem. B, **2005**, *109*, 11209.

11. G. Oskam, A. Nellore, R. L. Penn, P. C. Searson, J. Phys. Chem. B, **2003**, *107*, 1734.

12. K. Biswas, B. Das, C. N. R. Rao, J. Phys. Chem. B, **2008**, *112*, 2404.

13. M. B. Mohamed, Z. L. Wang, M. A. El-Sayed, J. Phys. Chem. A **1999**, *103*, 10255.

14. R. Seshadri, G. N. Subbanna, V. Vijayakrishnan, G. U. Kulkarni, G. Ananthakrishna, C. N. R. Rao, J. Phys. Chem. **1995**, *99*, 5639.

15. B. Abecassis, F. Testard, O. Spalla, P. Barboux, Nanolett. **2007**, *6*, 1723.

16. K. Biswas, N. Varghese, C. N. R. Rao, Small, **2008**, *4*, 649.

17. R. Viswanatha, S.Sapra, H. Amenitsch, B.Sartori, D. D. Sarma, J. Nanosci. Nanotech. **2007**, *7*, 1726.

18. R. Viswanatha, H. Amenitsch, D. D. Sarma, J. Am. Chem. Soc. **2007**, *129*, 4470.

19. R. Viswanatha, P. K. Santra, C. Dasgupta, D. D. Sarma, Phys. Rev. Lett. **2007**, *98*, 255501.

20. D. V. Talapin, A. L. Rogach, M. Haase, H. Weller, J. Phys. Chem. B **2001**, *105*, 12278.

21. R. Viswanatha, D. D. Sarma, Chem. Eur. J. **2006**, *12*, 180.

22. N. S. Pesika, Z. Hu, K. J. Stebe, P. C. Searson, J. Phys. Chem. B **2002**, *106*, 6985.

23. C. R. Bullen, P. Mulvaney, Nano Lett. **2004**, *4*, 2303.

24. W. W. Yu, X. Peng, Angew. Chem., Int. Ed. **2002**, *41*, 2368.

25. L. Qu, X. Peng, J. Am. Chem. Soc. **2002**, *124*, 2049.

26. Q. Dai, D. Li, H. Chen, S. Kan, H. Li, S. Gao, Y. Hou, B. Liu, G. Zou, J. Phys. Chem. B, **2006**, *110*, 16508.

27. E. M. Wong, P. G. Hoertz, C. J. Liang, B. Shi, G. J. Meyer, P. C. Searson, Langmuir **2001**, *17*, 8362.

28. U. K. Gautam, M. Rajamathi, F. Meldrum, P. Morgan, R. Seshadri, Chem. Commun., **2001**, 629.

29. U. K. Gautam, R. Seshadri, C. N. R. Rao, Chem. Phys. Lett., **2003**, *375*, 560.

30. C. B. Murray, D. J. Norrish M. G. Bawendi, J. Am. Chem. Soc. **1993**, *115*, 8706.

31. J. S. Pedersen, Adv. Colloid Interface Sci. **1997**, *70*, 171.

32. J. S. Pedersen, In Neutrons, X-rays and Light: Scattering Methods Applied to Soft Condensed Matter; Eds. P. Lindner, Th. Zemb, North-Holland: New York, **2002**, 391.

33. J. S. Pedersen, J. Appl. Crystallogr. **2004**, *37*, 369.

34. L. Rayleigh, Proc. Roy. Soc. London, Ser. A, **1911**, *84*, 25.

35. W. W. Yu, L. Qu, W. Guo, X. Peng, Chem. Mater. **2003**, *15*, 2854.

Chapter 4

Binding of DNA Nucleobases and Nucleosides to Graphene: A Preliminary Study

SUMMARY

This chapter of the thesis deals Isothermal Titration Calorimetric (ITC) investigations of the interaction of nucleobases and nucleosides with graphene. The strength of interaction of the nucleobases with graphene is found to vary in the order adenine (A) > cytosine (C) > thymine (T) in aqueous solutions and as guanine (G) > adenine (A) > cytosine (C) > thymine (T) when the nucleobases were dissolved in NaOH. In the case of the nucleosides, the strength of the interaction energy varies as adenosine > cytosine > thymidine.

.

4.1 Introduction

Graphene is a two dimensional material which is made of flat monolayer of carbon atoms packed into a honeycomb lattice. Graphene is a basic building block for graphitic materials of all other dimensionalities such as fullerenes (0D), carbon nanotubes (1D), and graphite (3D) and has started gaining importance very recently because of its unique properties [1]. The adsorption of biomolecules to graphene, carbon nanotubes and graphite surface has attracted few workers recently [2-8]. The binding energy of nucleobases with single walled carbon nanotubes is known to vary as guanine (G) > thymine (T) > adenine (A) > cytosine (C) [5]. The binding of nucleobases to graphene has been calculated theoretically and a comparison of the interaction strengths reported. For example, Gowtham et al. calculated the interaction energy of nucleobases using the plane-wave pseudopotential approach within the local density approximation (LDA) of density functional theory with graphene and found that the sequence of interaction energy changes as $G > T \approx C \approx A >$ uracil (U) [6]. Antony et al. have calculated the interaction energy of nucleobases graphene with the dispersion corrected density functional theory (DFT-D) method and found to vary in the order $G > A > T > C > U$ [7]. The single solute adsorption isotherm studies of the nucleobases at the graphite – water interface showed different adsorption behavior of the nucleobases to the graphite surface in the sequence $G > A > T > C > U$ [8]. We used to Isothermal titration calorimetry (ITC) to compare the binding of the nucleobases with graphene by measuring the heat associated with the interaction process. ITC is an ultrasensitive tool to study binding interactions in aqueous solutions. We carried out experiments in ITC with various nucleobases and graphene and the study gave the comparison of the interaction strengths of nucleobases as $G > A > C > T$.

4.2 Experimental section

Graphene was prepared from exfoliation of graphitic oxide by the method reported in the literature [9]. In this method, graphitic oxide was prepared by reacting graphite (Alfa Aesar, 2–15 mm) with a mixture of conc. nitric acid and sulfuric acid with potassium chlorate at room temperature for 5 days. Thermal exfoliation of graphitic oxide was carried out in a long quartz tube at 1050 °C under an argon atmosphere. The samples were characterized using X-ray diffraction (XRD) and Raman spectroscopy. In order to solubilize graphene in water, conc. nitric acid (2 mL), conc. sulfuric acid (2 mL) and water (20 mL) were added to graphene (10 mg) and subsequently heated in a microwave oven for 10 min under hydrothermal conditions. Further, the sample was heated at 100 °C for 12 h. The product was washed with distilled water and centrifuged repeatedly to remove traces of acid [10]. Finally graphene was dispersed in MilliQ water and this solution was used for further experiments.

ITC experiments were done with two different concentrations of graphene solutions such as 1.0mg/mL and 0.3mg/mL. Graphene was filled in the sample cell of isothermal titration calorimeter and reference cell was filled with MilliQ water. 10mM solutions of nucleobases (adenine, cytosine, thymine) were made in MilliQ water. In each experiment the 10μL of 10mM nucleobases solution take in the syringe was added in equal intervals of 3 minutes to the sample cell and heat changes for the additions was measured. Control experiments were performed by titrating nucleobases to MilliQ water under the same conditions and were subtracted with the experimental data to remove the dilution effect of nucleobases. To study the binding of the nucleosides (adenosine, cytidine, thymidine) to graphene ITC experiments were performed by titrating 10mM solutions of nucleosides

with graphene under the same conditions as that for nucleobases. Since guanine was insoluble in water, for comparison of the binding of all the four nucleobases, titrations were also performed using alkaline solutions of nucleobases (10mM solutions of nucleobases in 30mM NaOH) keeping all the other conditions same.

4.3 Results and discussion

The interaction of graphene with nucleobases was studied using ITC. Figure 4.1 shows the data recorded using ITC for various nucleobases with graphene. Figure 4.1 a, b, c shows the data for titrations of thymine, cytosine and adenine respectively to graphene with low concentration (0.3mg/mL) and d, e, f shows that for higher concentration of graphene (1mg/mL). Raw ITC data is plotted as the power in μcal/sec required to maintain both the cells at the same temperature versus time (each figure, top). The bottom of each Figure shows the integrated plot obtained by integrating each peak in the Raw ITC data and normalizing with respect to the concentration of nucleobases against the volume of the nucleobases added. The data were obtained after accounting for dilution effects of nucleobases and gives an idea about the heat liberated for each injection per mole of the nucleobases. The integrated plot in each figure clearly shows that the interactions are exothermic where exothermicity is reducing with progressive injections. The strength of interaction of nucleobases with graphene can be evaluated using the heat liberated during the initial stages of the interactions [5, 11]. This calculation gives the interaction energy of the nucleobases with graphene decreasing in the order A > C > T for both low and high concentration of graphene solution. Table 4.1 gives the approximate value of interaction energy obtained from the titrations in ITC.
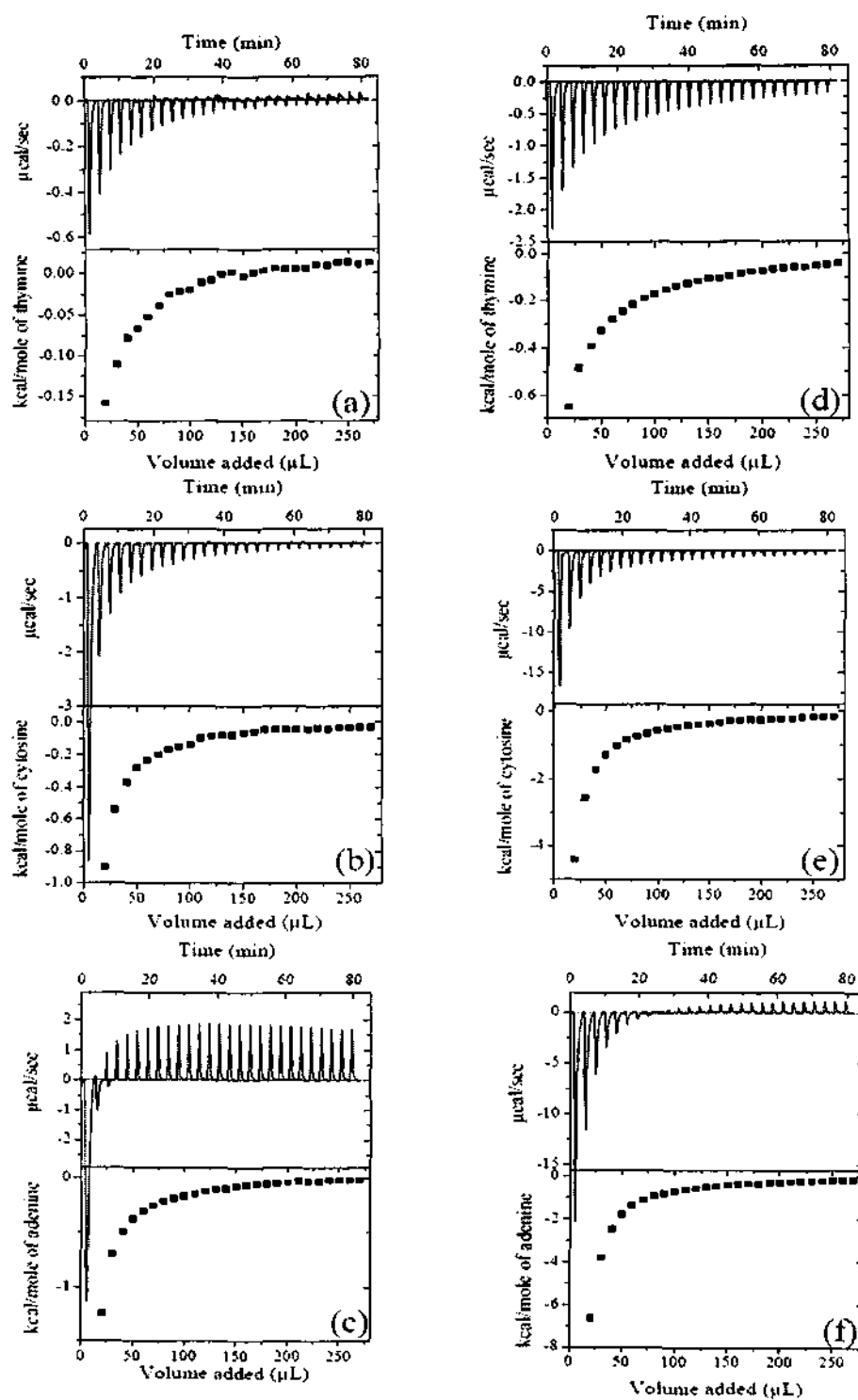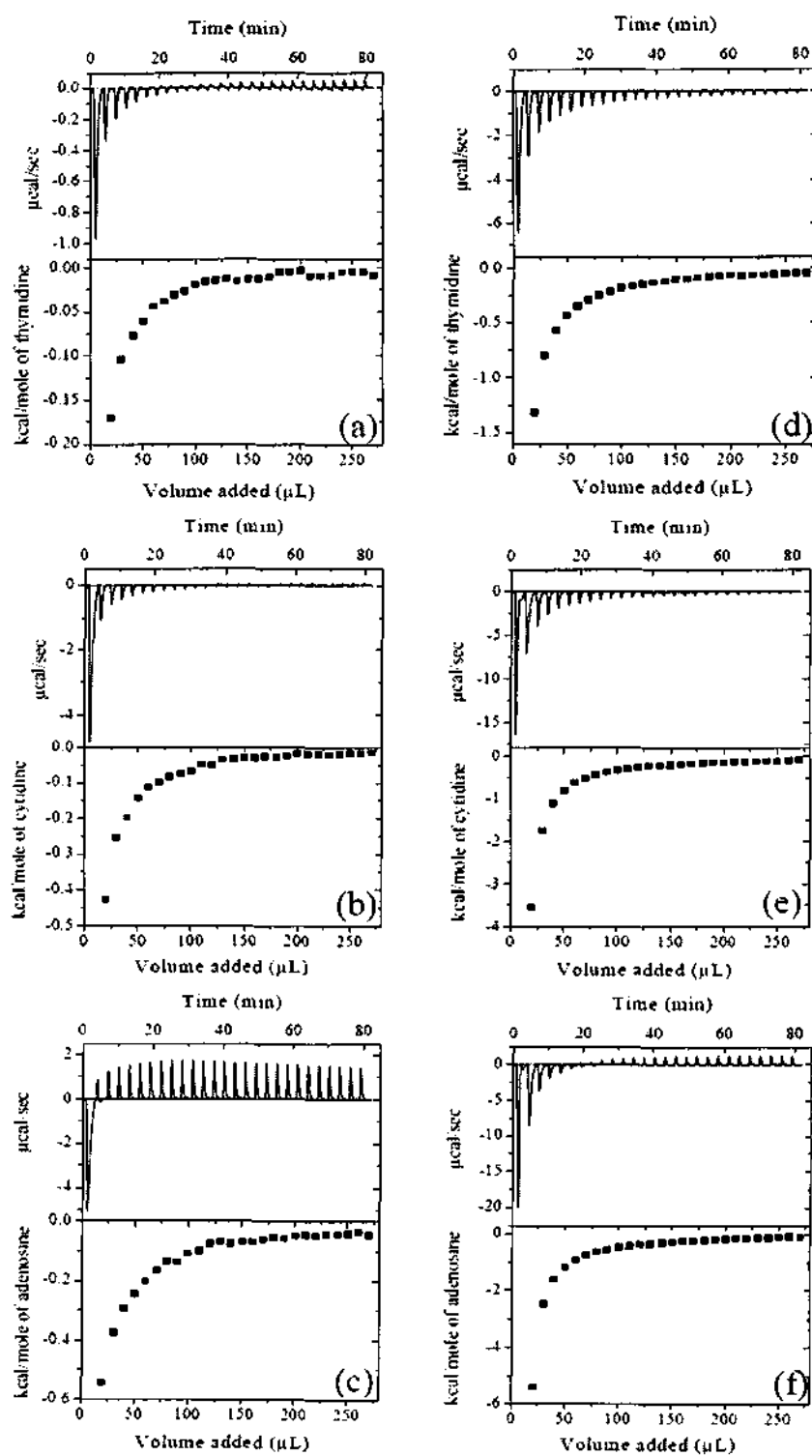
Figure 4.1: ITC data recorded for the interaction of nucleobases with graphene. Curves a-c corresponds to the titrations of nucleobases thymine (T), cytosine (C), adenine (A) with graphene (0.3mg/mL) and d-f gives the data for the same nucleobases (T, C, A) with graphene at higher concentration (1.0mg/mL)

Nucleobase	Graphene (0.3mg/mL)	Graphene (1.0mg/mL)
Thymine	-0.157	-0.65
Cytosine	-0.898	-4.395
Adenine	-1.249	-6.641

Table 4.1: Interaction Exothermicity for nucleobases in kcal/mol

The interaction of graphene with nucleosides was also studied by carrying out titrations in ITC under the same conditions as that for the nucleobases. Figure 4.2 shows the data recorded using ITC for various nucleosides with graphene. Figure 4.2 a, b, c shows the data for titrations of thymidine, cytidine and adenosine respectively to graphene with low concentration (0.3mg/mL) and d, e, f shows for the same nucleosides with higher concentration of graphene (1mg/mL). The data were obtained after accounting for dilution effects of nucleosides and gives an idea about the heat liberated for each injection per mole of the nucleosides. The strength of interaction of nucleosides with graphene can be evaluated as before. This calculation gives the interaction energy of the nucleosides with graphene decreasing in the order adenosine > cytidine > thymidine for both low and high concentration of graphene solution. Table 2 gives the approximate value of interaction energy obtained from the titrations in ITC.

Figure 4.2: ITC data recorded for the interaction of nucleosides with graphene. Curves a-c corresponds to the titrations of nucleobases thymidine, cytidine, adenosine with graphene (0.3mg/mL) and d-f gives the data for the same nucleosides with graphene at higher concentration (1.0mg/mL)

Nucleoside	Graphene (0.3mg/mL)	Graphene (1.0mg/mL)
Thymidine	-0.17	-1.311
Cytidine	-0.427	-3.542
Adenosine	-0.543	-5.401

Table 2: Interaction Exothermicity for nucleosides in kcal/mol

Since guanine (G) was insoluble in water we were able to compare the interaction strengths of only three nucleobases in aqueous solutions. Hence titrations with all the four nucleobases were done by dissolving the nucleobases in 30mM NaOH solutions keeping all the other conditions same and the results obtained are shown in Figure 4.3. This data gives a complete picture of the interaction strengths for the nucleosides in the order G > A > C > T. Table 4.3 gives an approximate value of interaction energy obtained from the titrations of nucleobases in alkaline solution with graphene (1mg/mL) in ITC.

Nucleobase	Graphene (1.0mg/mL)
Thymine	- 4.724
Cytosine	- 9.383
Adenine	- 11.846
Guanine	-13.452

Table 3: Interaction Exothermicity for nucleobases in NaOH in kcal/mol
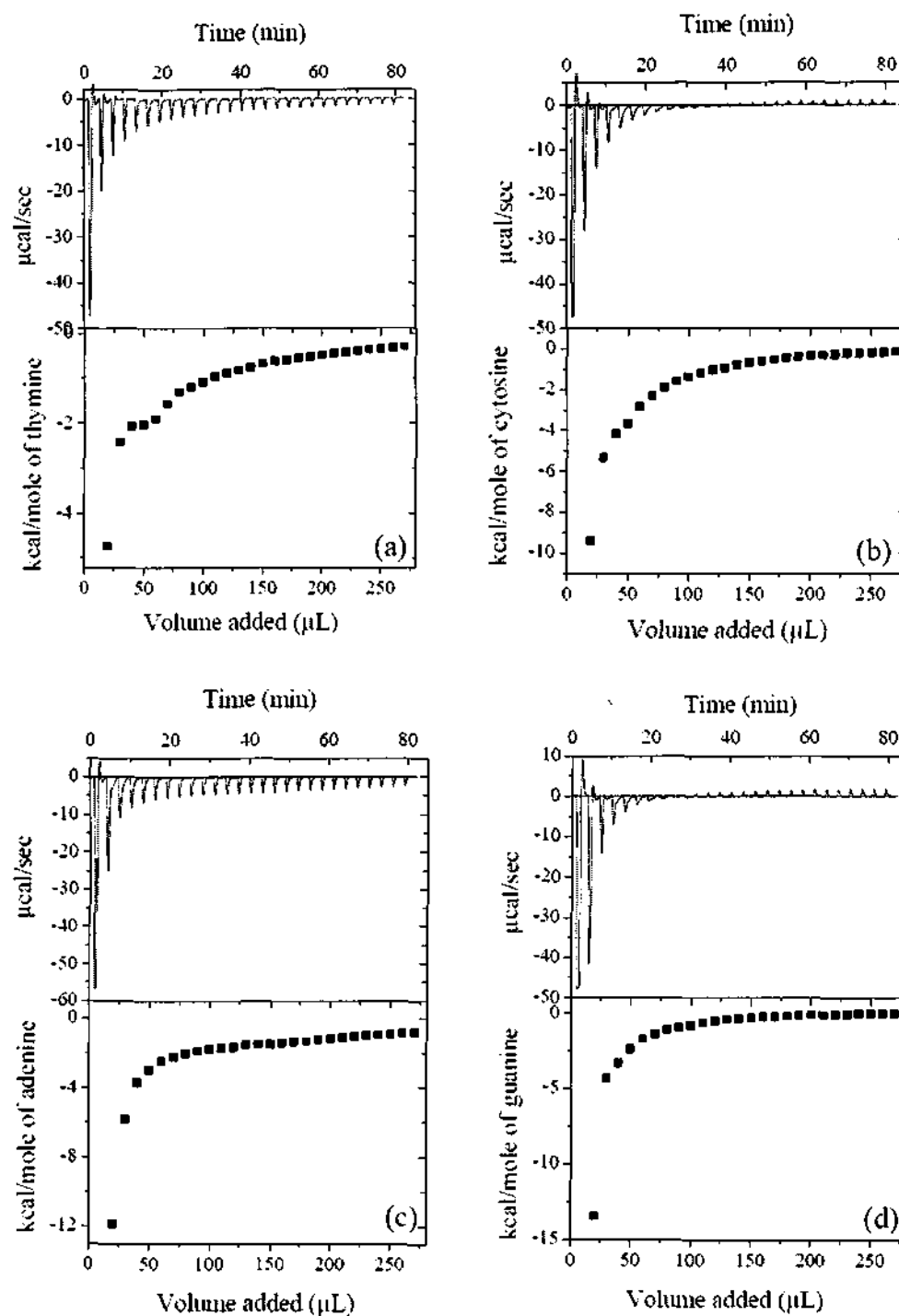
Figure 4.3: ITC data recorded for the interaction of nucleobases dissolved in 30mM NaOH with graphene. Curves a-d corresponds to the titrations of nucleobases thymine (T), cytosine (C), adenine (A) and guanine (G) with graphene (1.0mg/mL)

4.4 Conclusions

The strength of interaction of DNA nucleobases and nucleosides with graphene were calculated using experiments performed in the isothermal titration calorimetry. The data obtained from ITC helped us to compare the interaction energy of various nucleobases and nucleosides with graphene. The strength of interaction of the nucleobases decreases in the order A > C > T and for nucleosides it follows the order adenosine > cytosine > thymidine for experiments performed in aqueous solutions. The experiments with nucleobases in alkaline solution and graphene gave the strengths of interactions of all the four nucleobases with graphene in the order G > A > C > T.

References

1. A. K. Geim, K. S. Novoselov, Nat. Mater., **2007**, *6*, 183.

2. N. J. Tao, Z. Shi, J. Phys. Chem., **1994**, *98*, 1464.

3. T. Uchihashi, T. Okada, Phys. Rev. B., **1999**, 60, 8309.

4. J. E. Freund, M. Edelwirth, P. Krobel, W. M. Heckl, Phys. Rev. B., **1997**, 55, 5394.

5. A. Das , A. K. Sood, P. K. Maiti, M. Das, R. Varadarajan, C.N.R. Rao, Chem. Phys. Lett, **2008**, *453*, 266.

6. S. Gowtham, R. H. Scheicher, R. Ahuja, R. Pandey, S. P. Karna, Phys. Rev. B., **2007**, *76*, 033401.

7. J. Antony, S. Grimme, Phys. Chem. Chem. Phys., **2008**, *10*, 2722.

8. S. J. Sowerby, C. A. Cohn, W. M. Heckl, N. G. Holm, Proc. Natl. Acad. Sci., **2001**, *98*, 820.

9. H. C. Schniepp, J.-L. Li, M. J. McAllister, H. Sai, M. Herrera-Alonso, D. H. Adamson, R. K. Prudhomme, R. Car, D. A. Savilleand, I. A. Aksay, J. Phys. Chem. B, **2006**, *110*, 8535.

10. K. S. Subrahmanyam, S. R. C. Vivekchand, A. Govindaraj, C. N. R. Rao, J. Mater. Chem., **2008**, *18*, 1517.

11. A. Gourishankar, S. Shukla, K. N. Ganesh, M.Sastry, J. Am. Chem. Soc., **2004** , *126*, 13186.

620. 5

P08

Recd. on 21/7/08